Comprehensive characterization of particulate matter emissions produced by a liquid-fueled miniCAST burner

Mouad Daoudi, Philipp Schiffmann, Alessandro Faccinetto, Arnaud Frobert, Pascale Desgroux

Comprehensive characterization of particulate matter emissions produced by a liquid-fueled miniCAST burner

Aerosol Science and Technology, 2023, 57 (9), pp.872-889.

DOI⟨10.1080/02786826.2023.2228372⟩. ⟨hal-04268670⟩

Mouad Daoudi [a,b], Philipp Schiffmann [a], Alessandro Faccinetto [b], Arnaud Frobert [a], Pascale Desgroux [b]

[a] IFP Energies Nouvelles, Institut Carnot IFPEN TE, France

[b] Univ. Lille, CNRS, UMR 8522 - PC2A - Physicochimie des Processus de Combustion et de l'Atmosphère, Lille F-59000, France

Corresponding author: pascale.desgroux@univ-lille.fr

Abstract

Soot particles generated by a liquid-fueled miniCAST burner, supplied with diesel B7, was characterized for the first time over a total of 34 operating points covering an overall equivalence ratio (ϕ) range of 0.103-1.645. To characterize the gas and particulate phase emissions, electron microscopy images, mobility-equivalent size distributions and mass concentration of the soot aggregates were recorded, and optical extinction/absorption coefficients of the exhaust were measured. The burner produces soot aggregates with geometric mean diameter size in the range 45-105 nm with primary particle size in the range 18-39 nm. The Ångström absorption exponent (α) was evaluated in the range 400-1000 nm and was found to increase with ϕ and vary in the range 1.05-2.25. The interposition of a catalytic stripper in the sampling line was found to (i) flatten the shape of the size distribution of aggregates, (ii) oxidize most of the gas phase thus impacting optical extinction coefficients particularly below 400 nm and (iii) decrease α. The soot volume fraction (f_v) was determined by three independent methods: optical absorption, mass deposit and mobility size distribution combined with morphology data. f_v evaluated from size mobility data accounting for morphological aspects agreed within 13 % with f_v measured optically and within 25 % with f_v evaluated from mass concentration measurements. The precise methodology developed to characterize engine-like soot particles produced by a liquid-fueled miniCAST can now be transposed to study other regular, renewable, and surrogate liquid fuels to investigate their physical and optical properties before considering their large-scale use.

Keyword

MiniCAST, aerosol characterization, aggregate morphology, optical extinction, soot volume fraction, catalytic stripper.

1. Introduction

Much of the interest around particulate matter (PM) emission control stems from the adverse effects they can have on human health (Bourdrel et al. 2017; Kopnina 2016; Ranft et al. 2009; Bernstein et al. 2004; Pope III et al. 2002), particularly in urban areas (Gonzalez 2020). This is due to their high specific surface, content of hazardous molecules and micrometric size, hence the use of indicators such as PM_{10} and $PM_{2.5}$ for air quality monitoring. The presence of PM in ambient air has also important drawbacks on environment and on climate as they are considered to be the second most important emissions after CO_2 (IPCC 2022; Bond et al. 2013; Jacobson 2001). In particular, PM impact the atmosphere radiative exchange in various ways (Kärcher 2018; Popovicheva and Starik 2007; Schumann 2005; Seinfeld 1998), hence the need for them to be monitored.

As the world's population grows, and passenger and freight travel expand, the use of petroleum derivatives for internal combustion engines is expected to continue to grow to fulfill the demand for the next 30 years (U.S. Energy Information Administration 2021). This means that the fuel choice is important to lower global pollutant and greenhouse gas emission levels. For instance, alternative fuels with lower carbon emission potential are extensively researched. This is the case of bio- or e-fuels alone or blended with fossil fuels. Using such fuels can be advantageous since they are compatible with today's engine technologies. On the other hand, the use of new fuels might have an impact on pollutants and PM emissions. The PM generated from the combustion of alternative fuels need to be characterized and closely monitored before these fuels are mass-produced.

To characterize the nature of PM emissions from various combustion sources, laboratory PM sources capable of burning different fuels are needed. Using an engine for such purpose is expensive, complex and does not permit to easily change the emission characteristics. In this regard, diffusion or premixed flames generated in laboratory environment using well documented reference burners such as the McKenna burner (Ghazi et al. 2013; Migliorini et al. 2011; Yon et al. 2011) or the Santoro burner (Kelesidis and Pratsinis 2022; Santoro and Miller 1987; Santoro et al. 1983) offer an easier control. These burners were, and continue to be, used to study the soot particles formation process and they can be used for the calibration of

measurement systems. However, soot generators are often preferred outside academia since they are much easier to use and operate. In particular, during the last two decades, the so-called miniCAST soot generators (from Jing Ltd., Switzerland) have been widely used to generate soot aggregates (Ess et al. 2021; Malmborg et al. 2019; Marhaba et al. 2019; Saffaripour et al. 2017; Bescond et al. 2016; Durdina et al. 2016; Kim et al. 2015; Moore et al. 2014; Mamakos et al. 2013; Schnaiter et al. 2006) to serve as calibration aerosols, yet they are limited by design to a single gas fuel (i.e., propane).

To burn diesel-like fuels, the more recent diesel miniCAST was developed (Mueller et al. 2016). A number of other commercial soot generators have been recently under investigation such as the miniature inverted soot generator (from Argonaut Scientific Corp., Canada) (Bischof et al. 2020; Kazemimanesh et al. 2019; Moallemi et al. 2019) that allows the use of ethylene, propane, ethane or fuel blends with methane and nitrogen. So far, soot aggregates produced by propane miniCAST have been extensively studied on many aspects (Ess et al. 2021; Malmborg et al. 2019; Marhaba et al. 2019; Saffaripour et al. 2017; Bescond et al. 2016; Durdina et al. 2016; Kim et al. 2015; Moore et al. 2014; Mamakos et al. 2013; Schnaiter et al. 2006) and have shown similar characteristics to soot produced by engines or aircraft (Marhaba et al. 2019; Moore et al. 2014). However, while the propane miniCAST is able to provide engine-like soot aggregates, it does not meet the need for evaluating PM characteristics when other fuels are used, particularly diesel, kerosene or biofuels. To the best of the authors knowledge, the only available published literature on this diesel miniCAST (Mueller et al. 2016) focused on studying the impact of fuel additives on the chemical composition of soot aggregates. Overall, there seems to be a significant lack of information on soot aggregates generated using liquid fuels.

To determine the physical properties of soot aggregates using a variety of liquid fuels, this article first proposes a protocol to characterize the emissions of a diesel miniCAST, and then applies said protocol to 34 different operating points, therefore setting a reference mapping for liquid-fueled miniCASTs. This characterization involves the measurement of size distributions (using scanning mobility particle sizer), morphology (using electron microscopy), soot volume fraction and optical extinction coefficients. Consequently, a detailed database is provided which can be valuable for future use. Additionally, this article evaluates the impact of the thermal treatment using a catalytic stripper (CS) on PM to understand the impact of oxidizing volatile

PM (vPM) on the optical properties of combustion exhaust. Additionally, since emission thresholds set by the current regulations concern only non-volatile PM (nvPM), that can contain organic and inorganic material, the use of the CS on diesel miniCAST exhaust allows using this burner to produce nvPM for calibration purposes. Finally, the soot volume fraction is determined by comparing three procedures based on mobility size distribution accounting for morphological aspects of the soot aggregates, mass concentrations and spectral light extinction taking into account scattering and gas phase absorption.

2. Experimental setup

A dedicated test bench was built around a liquid-fueled miniCAST fed with diesel B7 as schematized in Figure 1. The chemical composition of liquid diesel B7 is given in Table R.1 (see supplementary information S.1). In this setup, the diesel miniCAST produces an exhaust flow of ~ 30 L/min. This exhaust is sent through a main vein where it is further diluted with air at atmospheric pressure. The following sections describe in more detail the instrumentation used to pretreat, sample and characterize the exhaust.

[Figure 1 near here]

2.1. Exhaust from miniCAST burner

2.1.1. Exhaust generation

A miniCAST burner model 5102 D (Jing Ltd., Switzerland) for liquid fuels is used to produce soot aggregates. Figure 2 illustrates the dual burner design where the liquid fuel is preheated by a lower non-sooting C_3H_8/air heating flame (1) and burns in a diffusion sooting flame (2) in the upper part of the burner.

[Figure 2 near here]

The upper flame is fueled by two coaxially arranged vertical tubes carrying in the center a C_3H_8/air mixture and in the peripheral tube the liquid fuel. The lower flame (1) is fueled by a homogeneous mixture of 30 mL/min of C_3H_8 and 300 mL/min of air and is used for pre-heating the liquid fuel routed through the annular space. The central tube is used to deliver a C_3H_8/air mixture (10 mL/min of C_3H_8 with 20 mL/min of mixing air) to sustain the idle flame on the

burner's top, which provides the ignition for the sooting flame supplied with the liquid fuel as shown in Figure 2. Upon each use, a 30 minutes warm-up period during which the burner runs under idle condition is needed to establish a thermal steady state for the system. During this time, the oxidation air flow rate is by default set to 3 L/min to provide enough oxygen for the complete combustion of the heating flame. Once ready, mixing air and oxidation air flow rates can be tuned in the ranges 10-250 mL/min and 1-3 L/min, respectively. By adding the desired liquid fuel flow rate, the idle flame on the top of the burner is replaced by a bright yellow sooting flame (2). To quench residual reactivity and limit particle coagulation, the exhaust is diluted at the tip of the flame using a 7.5 L/min of N_2. A subsequent dilution with 20 L/min of filtered air further reduces particle coagulation. The factory mass flow controller (e.g., mini-CORI-FLOW) for liquid fuel is limited to 70 µL/min and was found to be a major source of flame instability. To improve test-to-test repeatability, the mass flow controller was replaced with a syringe pump model P-500 (Pharmacia biotech., U.S.A) to deliver precise and constant liquid fuel flow allowing both a wider and stable operating range between 0 and 250 µL/min. In this work, the European standard fuel for light duty vehicles diesel B7 (EN 590 2022) was used over the entire operating range.

2.1.2. Operating points

Overall, 34 operating points (OPs) were investigated (see supplementary information Table S.1.1). Among these OPs, focus was brought on fully characterizing six of them, whose settings are summarized in Table 1. The OPs are chosen to be quasi-evenly spaced within the explored range of stable operating conditions in terms of the flame overall equivalence ratio (ϕ) in 0.103-1.645. ϕ is calculated from the ratio of the experimental (Exp.) and stoichiometric (Stoich.) fuel/air mass flow rate ratios using $\phi = \left(\dot{m}_{fuel}/\dot{m}_{air}\right)_{Exp.} / \left(\dot{m}_{fuel}/\dot{m}_{air}\right)_{Stoich.}$ with $\dot{m}_{fuel}$ being the fuel mass flow rate and $\dot{m}_{air}$ the air mass flow rate and by considering $C_{14.5}H_{26.7}O_{0.1}$ as the average chemical formula for diesel B7.

These six OPs (OP2, OP9, OP17, OP27, OP32 and OP34) were fully characterized in terms of particle size distribution, morphology, soot volume fraction and optical extinction coefficients. Only mobility size distribution and light extinction measurements were performed on the remaining 28 OPs.

[Table 1 near here]

2.1.3. Exhaust aftertreatment

As the exhaust left the burner, ~ 554 L/min of dry filtered air at ambient temperature was added in the first external dilution stage resulting in ~ 19:1 dilution ratio (volumetric). The exhaust was then sampled from the main vein: (1) untreated. (2) filtered using a microfiber "particle filter" (model DIF.5K, Classic Filters Ltd., U.K), to remove particles and allow to study gas phase independently. (3) treated using a "catalytic stripper" (CS, model CS-015 Catalytic Instruments GmbH., Germany) as shown in Figure 1. The CS, operated at 1.5 L/min nominal flow rate and 350 °C, was used to study the impact of volatile organic compounds (VOCs) on the exhaust properties. Unless mentioned otherwise, the diagnostics described in the following sections are all done on the exhaust sampled at the same dilution ratio (~ 19:1) and have passed through the same sampling lines. If soot aggregates coagulation along the sampling line occurs, this is not a problem as long as all diagnostics are performed at the same location downstream the sampling line (see supplementary information S.1) on the same volume sample.

2.2. Diagnostics setup

Size measurement (SMPS): The mobility-equivalent size distributions of soot aggregates were measured in the range 6-224.7 nm over a scanning period of 120 s of stable soot generation. This scanning mobility particle sizer (SMPS) combines an electrostatic classifier 3080 (TSI Inc., U.S.A), a L-DMA column 3081 (TSI Inc., U.S.A), along with an X-ray neutralizer 3088 (TSI Inc., U.S.A) and a CPC 3775 (TSI Inc., U.S.A). The sheath flow rate, the inlet flow rate and the impactor nozzle size were set to 15 L/min, 1.5 L/min (10:1 ratio) and 0.071 cm, respectively. For each OP, the size distributions were measured three times in a row, therefore providing statistics on soot aggregates number concentration (PN), mobility-equivalent geometric mean diameter ($D_{geo,m} = \exp\left(\frac{\sum_i^k N_i \ln D_{m,i}}{PN}\right)$, with N_i and $D_{m,i}$ the number concentration and mobility diameter of

each class of size i, respectively) and geometric standard deviation (σ_{geo,D_m}) provided by the device software (AIM 9.0, TSI Inc., U.S.A). The multiple charging correction integrated in the software was used for all experiments. The losses in the sampling line by diffusion were neglected and the mobility size distributions were visualized in normalized concentration $dN/dlogD_m$.

Mass measurement: For PM mass measurement, PM deposit on Pallflex-Emfab borosilicate microfibers filters (Pall Corp., U.S.A) were carried out using an automated antistatic micro tunnel sampler as shown in Figure 1. Before using the filters, they were first heated for 4 hours at 180 °C and left to cool overnight at room temperature in a particle-free environment. The exhaust was then sampled at Q = 1.5 L/min over $\Delta t = 10$ min. Using an XP6 microbalance (Mettler Toledo Inc., U.S.A) ($\pm$ 0.4 µg repeatability), the weight of the filters was measured prior to sampling and after 4 hours resting period during which they were stored in a particle-free environment at ambient temperature. Soot deposits mass (Δm) was then deduced and soot mass concentration $C_s = \Delta m/\Delta t \times Q$ calculated, where C_s is the total mass concentration containing both nvPM and (condensable) vPM.

Electron microscopy imaging (TEM): To acquire more information on the morphology of soot aggregates, electron microscopy images were recorded. For these experiments, a second dilution stage (resulting in ~ 220:1 dilution ratio) located further down the line was deemed necessary to avoid overloading the sampling grids. This second dilution was done using an ejector diluter model DI-1000 (Dekati Ltd., Finland) operated using N_2 as a dilution gas, to sample 1.5 L/min from the exhaust to be compatible with both CS and SMPS nominal flow rates. Once the exhaust was diluted, soot aggregates were probed downstream the second dilution stage using a mini particle sampler (MPS, Ecomesure, France) as they crossed a perforated 400 mesh Au holey carbon film (Agar Scientific Ltd., U.K) TEM grid located halfway the MPS tube. This sampling was operated at 20 mL/min using a Gilian air sampling pump model GilAir Plus (Sensidyne LP., U.S.A) positioned downstream the MPS tube while varying sampling time between 10 s and 40 s (see supplementary information Table S.3.2).

The loaded TEM grids were then analyzed, within two weeks after their preparation, to acquire scanning transmission electron microscopy (STEM) images on a Nova Nano SEM 450

microscope operated with an acceleration voltage of 30 kV and using STEM II detector with bright field detection under immersion mode and 6 µs scanning time. On average, 20 STEM images, each having a size of 1536 ×1024 pixels, were acquired at fixed magnification (× 60.000), making the optical resolution of ~ 1.4 nm/Pixel. These images were then processed to evaluate soot aggregates morphological key parameters (see supplementary information S.3). For a more detailed characterization, transmission electron microscopy (TEM) images were acquired. This was done using JEM, models 2100F or F200 (JEOL Ltd., Japan), microscopes operated with an acceleration voltage of either 200 kV or 80 kV, respectively. A lower acceleration voltage was deemed necessary, particularly for fuel-rich OPs, to stabilize the specimen during the image acquisition process.

Light extinction measurement: Optical extinction coefficients were measured inside an optical extinction cell over the 200-1000 nm wavelength range with a 1.5 nm resolution. This was done using a continuous deuterium-halogen light source model DH 2000 (Ocean Optics Inc., U.S.A) that emits in the UV, visible and near-IR range a spectrum on one side of the cell while the transmitted spectrum was analyzed on the opposite end with a Q-mini, model wide UV (Broadcom Inc., U.S.A) spectrometer. The spectrometer has a 20 µm entrance slit, 300 lines/mm transmission grating, 50 mm focal length and uses a 2500-pixel linear CCD sensor. The single pass extinction cell is made of a stainless-steel tube (L = 1 m long, 4 mm inner diameter) and 1.5 L/min of exhaust gases passed through it. Optical connection on both ends were done using a 10 mm focal length collimating lens, model 74-UV (Ocean Optics Inc., U.S.A) and a QP-450-0.25-XSR optical fiber (Ocean Optics Inc., U.S.A). The intensity of transmitted light crossing the exhaust $I_t(\lambda)$ was recorded with 40 ms exposure time and was performed simultaneously to SMPS size distribution measurements. The choice of 40 ms exposure time lays within the linear behavior of the spectrometer. During post-processing, the spectra were averaged over ~ 400 s which is the time needed to acquire 3 consecutive size distribution measurements. A reference baseline was measured on a clean air flow, before and after each recording. The optical extinction coefficients were calculated using Beer-Lambert law (Swinehart 1962) $K_{ext} = -\frac{1}{L}\ln(I_t(\lambda)/I_0(\lambda))$. Care was taken to avoid lens fouling by cleaning the optical cell upon changing each OP. For both short (< 20 minutes) and long (up to 90 minutes) periods of time,

soot PN production was considered to be stable when the standard deviation on the concentration was < 10 % of the measured value (see supplementary information Figure S.1.2).

3. Results and discussions

The results discussed here focus on the capabilities of the liquid-fueled miniCAST burner supplied with diesel B7 in terms of generating soot aggregates of controlled size distribution, morphology and optical extinction coefficient under various operating conditions (section 3.1). Then, this study aims to retrieve key parameters that are necessary to evaluate the soot volume fraction used as metric to compare size, mass and optical diagnostics (section 3.2).

3.1.Characterization of soot aggregates

Soot aggregates can be described in many ways. Here, it is proposed to describe and compare soot aggregates number concentration, size, morphology and polydispersion for all 34 OPs for untreated exhaust, based on SMPS and TEM analyses and optical properties for OP2, OP9, OP17, OP27, OP32 and OP34. The impact of using the CS is examined on each of those aspects.

3.1.1. Size distributions

Impact of the miniCAST flow rates: Focusing first on untreated exhaust, a parametric study was carried out to evaluate the diesel miniCAST ability of generating soot aggregates with controlled number concentration (PN), mobility-equivalent geometric mean diameter ($D_{geo,m}$) and geometric standard deviation (σ_{geo,D_m}). To make the comparison of different OPs possible, care was taken to ensure that all measurements could be performed with the same dilution conditions. A compromise had to be found between avoiding the saturation of the SMPS for the rich OPs and being sensitive enough to detect soot light attenuation for the lean OPs. The choice of ~ 19:1 dilution ratio made that compromise possible. As a result, the PN number for some of the richest OPs is slightly above the saturation threshold of the SMPS neutralizer as recommended by TSI ($<10^7$ cm^{-3}). As the impact on the calculation of f_v was verified to be limited, this approach was considered acceptable to ensure that all measurements could be performed with the same dilution (see also supplementary information S.1). This study showed

that, at fixed oxidation air flow rate (2 L/min), soot PN increased from $\sim 0.5 \times 10^7$ cm^{-3} up to $\sim 1.8 \times 10^7$ cm^{-3} (Figure 3.a) while $D_{geo,m}$ decreased from ~ 90 nm down to ~ 55 nm (Figure 3.b) with ϕ. For σ_{geo,D_m}, no obvious trend was observed (Figure 3.c). These observations remained valid regardless of the mixing air flow rate choice, suggesting that the latter has no significant impact over aggregates number concentration, size or polydispersion. In a second parametric study, the mixing air flow rate was kept constant (0.1 L/min) and decreasing the oxidation air flow rate, going from fuel-lean to fuel-rich conditions, made soot PN increase from $\sim 0.3 \times 10^7$ cm^{-3} up to $\sim 1.8 \times 10^7$ cm^{-3} (Figure 3.d). Meanwhile, soot aggregates were observed to grow in size from ~ 45 nm up to a maximum of ~ 105 nm around ϕ ~ 0.4 before decreasing down to ~ 60 nm for ϕ > 1 (Figure 3.e).

Using a propane miniCAST, Moore et al. 2014 observed a similar trend, except that the aggregate size reached a maximum under slightly fuel-lean conditions before starting decreasing under fuel-rich conditions, therefore covering the range 10-130 nm in modal diameters. We attribute this difference to the fuel (propane vs. diesel B7) and to the burner's geometry. When decreasing the oxidation air flow rate in the diesel miniCAST, σ_{geo,D_m} exhibited two distinct behaviors: at a lower liquid fuel flow rate (50 µL/min), σ_{geo,D_m} decreased rapidly (Figure 3.f) and at a higher liquid fuel flow rate (200 µL/min), σ_{geo,D_m} remained quasi-constant at ~ 1.7. Overall, σ_{geo,D_m} was found to vary between 1.5 and 1.8. This range of variation is similar to what was observed for soot aggregates generated by a propane miniCAST, for which σ_{geo,D_m} was reported to vary between 1.6 and 1.8 (Saffaripour et al. 2017). All these observations demonstrate the ability of the diesel miniCAST to produce soot aggregates at variable sizes and concentrations by controlling only three flow rates (oxidation air, mixing air and liquid fuel flow rates) hence offering the user a panel of choices. Soot production repeatability is discussed in supplementary information S.1

[Figure 3 near here]

Impact of the catalytic stripper: Mobility-equivalent size distributions averaged over 3 consecutively measured size distributions representing OP2, OP9, OP17, OP27, OP32 and OP34 are shown in Figure 4. Figure 4.a shows these size distributions for untreated exhaust while Figure 4.b displays their corresponding CS-treated ones. Looking at Figure 4.b, one can observe

that regardless of the OP, using the CS affects the shape of the size distributions that looks more flattened. To examine in detail how the CS affects the soot aggregates size distribution descriptors (PN, $D_{geo,m}$ and σ_{geo,D_m}), the same parametric study discussed in the beginning of this section was conducted on all 34 OPs. The results are shown in supplementary information Figure S.2.1. This information is important because the thresholds set by current emission regulations such as Euro 6d-temp (EU 2020) concerns only nvPM above 23 nm that survive oxidation at 350 °C. Applying the CS thermal treatment at that temperature allows to examine the size distributions of nvPM produced by the diesel miniCAST which can be used for calibration purposes.

[Figure 4 near here]

Overall, almost all variations in PN, $D_{geo,m}$ and σ_{geo,D_m} previously described for the untreated exhaust remain valid for the CS-treated one. The only exception concerns σ_{geo,D_m} at fixed mixing air at 0.1 L/min at a higher liquid fuel flow rate (200 µL/min) for which σ_{geo,D_m} was observed to increase from 1.7 to 1.8 instead of remaining quasi-constant at ~ 1.7 for the untreated condition. It should be clarified that in this work, for each OP the CS was used on the entire aggregates size classes without any prior size selection. Using measured PN, $D_{geo,m}$ and σ_{geo,D_m} for all 34 OPs for both untreated and CS-treated exhaust, the variation from untreated to CS-treated condition is calculated for each of those parameters. At fixed oxidation air (2 L/min) PM crossing the CS saw their $D_{geo,m}$ shift (by up to 20 %) toward lower sizes as ϕ increased, while at fixed mixing air (0.1 L/min) under fuel-lean conditions $D_{geo,m}$ was not much affected. Using the CS also results in PN losses. In this regard, it is proposed to evaluate the particle penetration measured in this work and compare it with the one accounting for diffusion and thermophoretic losses as proposed by the manufacturer (Catalytic Instruments GmbH & Co.KG 2020) and which are expected to be size dependent. Contrarily to PN losses, the particle penetration refers to the amount of PN able to cross the CS compared to the case where the CS is bypassed. Again, since for each OP the CS was used on the entire aggregates size classes without any prior size selection, the choice was made to consider particle penetration as a function of $D_{geo,m}$ measured when the CS was bypassed. For the soot aggregates investigated here this particle penetration is found to fluctuate in the range 60-80 % which is in good agreement with

the solid particle penetration provided by the manufacturer (Catalytic Instruments GmbH & Co.KG 2020) even though it was obtained for size selected silver spherical particles and was expected to vary in the range 70-74 % for sizes in the range 45-105 nm.

Fit of the size distribution: To minimize the diffusion losses, the SMPS was operated in high flow mode (1.5 L/min, 1:10 sample: sheath flow ratio, 6-224.7 nm range). As a result, for some OPs the upper tail of the size distributions appears to be truncated as shown in Figure 4.a. If the soot volume fraction (f_v) was evaluated considering solely the measured size distribution, f_v would be underestimated because of the missing large diameter values. To overcome this lack of information, f_v was calculated using the fitting probability density function (PDF) extrapolated to zero probability at high D_m rather than the measured data. Aerosol size distributions are well described with log-normal PDF (Eq.1).

$$n(D) = \frac{dN}{dD} = \frac{1}{D \ln(\sigma_{geo,D_m})\sqrt{2\pi}} e^{-\frac{\left(\ln\left(\frac{D}{D_{geo,m}}\right)\right)^2}{2\ln(\sigma_{geo,D_m})^2}} \quad \text{(Eq.1)}$$

This observation is merely empirical but has the benefit of describing a size distribution using only three parameters (PN, $D_{geo,m}$ and σ_{geo,D_m}). However, assuming that a size distribution follows a log-normal PDF may yield erroneous values particularly for distribution moments higher than the second order (Sorensen 2001) such as f_v which is a 3rd order moment (Greenberg and Ku 1997). Figure 5.a shows an example of a log-normal PDF that is not accurate (R^2 = 0.87, black bold dotted line). In this case, a bi-modal log-normal PDF was found to render a better fit (R^2 = 0.99, green solid line). On the other hand, Figure 5.b shows an example where a monomodal log-normal PDF function is accurate enough (R^2 = 0.99, black bold dotted line). Either way, for all size distributions the PDF (monomodal or bimodal log-normal) that renders the best fit is considered to extrapolate the size distribution tail as illustrated in Figure 5.

[Figure 5 near here]

3.1.2. Morphology

Impact of the miniCAST flow rates: STEM and TEM images of soot aggregates, shown in Figure 6, were taken for the six investigated OPs (OP2, OP9, OP17, OP27, OP32 and OP34), and reveal morphological changes between fuel-lean and fuel-rich conditions. Although all detected soot particles are fractal-like aggregates, TEM shows that under fuel-lean conditions (OP2, OP9, OP17 and OP27) the primary particles have more clearly perceptible edges than under fuel-rich conditions (OP32 and OP34).

[Figure 6 near here]

The morphology of soot aggregates is usually described using the so-called fractal law linking the number of primary particles per aggregate (N_p) to primary particle diameter (D_p) and to the particle gyration diameter (D_g). The determination of D_g is detailed in supplementary information S.3 (fractal analysis subsection). This power law (Eq.2) introduces a fractal prefactor (k_f) and a fractal dimension (D_f) (Köylü et al. 1995).

$$N_p = k_f \left(\frac{D_g}{D_p} \right)^{D_f} \quad \text{(Eq.2)}$$

The second part of this analysis focuses on the assessment of morphological parameters that was performed *a posteriori*, by analyzing STEM images. The analysis was performed on isolated aggregates selected on the STEM images. This consisted of segmenting raw STEM images into single binary aggregates (see supplementary information Figure S.3.2) which was done using a semi-automated method (Sipkens and Rogak 2021; Sipkens et al. 2021) to overcome background-related issues as it allows the user to intervene when necessary to help indicate an aggregate border. On average, more than 150 aggregates per sample were successfully retrieved. Compared to similar studies (Sipkens and Rogak 2021; Marhaba et al. 2019; Bescond et al. 2014; Mamakos et al. 2013; Ouf et al. 2010) this is considered statistically sufficient. Euclidian Distance Mapping - Surface Based Scale (EDM-SBS, Bescond et al. 2014) was then applied on each aggregate (see supplementary information Figure S.3.3) providing information encompassing scales encountered in each single aggregate (see supplementary information

Figure S.3.4). That same information was then interpreted to evaluate the geometric mean diameter ($D_{geo,p}$) and geometric standard deviation (σ_{geo,D_p}) of the primary particles following a real soot-based calibration approach (Bescond et al. 2014). Finally, with the help of correlations (see supplementary information S.3) expressing N_p as a function of aggregate and primary particles projected areas (Sorensen and Roberts 1997; Köylü et al. 1995), a fractal analysis was conducted to evaluate D_f and k_f (see supplementary information Figure S.3.5).

[Table 2 near here]

The results, summarized in Table 2, show that overall $D_{geo,p}$ increased from 18.0 nm up to 39.2 nm when the burner was switched from fuel-lean to fuel-rich conditions, while σ_{geo,D_p} was observed to slightly decrease from 1.580 down to 1.394. D_f and k_f showed no obvious trend and were observed to vary in the ranges 1.805-1.941 and 1.960-1.988, respectively. These values are similar to the ones reported for soot aggregates produced by propane miniCAST (Bescond et al. 2016). These results are in agreement with engine-like aggregate whose mean primary particle diameter and fractal dimension are generally found to vary between 10 nm and 40 nm and between 1.5 and 2.2, respectively (Lapuerta et al. 2006, 2020; Cadrazco et al. 2019; Soriano et al. 2017; Ye et al. 2016; Agudelo et al. 2014; Li et al. 2011). For the sake of simplicity, primary particles are from now on considered monodisperse with a mean primary particle diameter $\overline{D_p} \approx D_{geo,p}$.

Impact of the catalytic stripper: When the CS was used, $D_{geo,p}$ and σ_{geo,D_p} were found similar to those obtained for the untreated aggregates (see Table 2). This suggests that the CS thermal treatment does not have a major impact on monomer size or polydispersion, at least not a clearly visible impact with such diagnostics. On the other hand, it was observed that the primary particles boundaries became more noticeable under CS-treated fuel-rich condition OP34 compared to their respective untreated ones, while remaining fairly similar under OP9 and OP27 (see supplementary information Figure S.3.6). This might suggest that a significant amount of condensed semi-volatile organic compounds might be overlayed all over the aggregate surface and that was partially removed once heated at 350 °C. This is still to be confirmed using adequate tools describing accurately the chemical composition of soot surface.

3.1.3. Optical extinction coefficients

In this section, the optical extinction coefficients (K_{ext}) is measured for the miniCAST exhaust under various conditions. Starting with the untreated exhaust, Figure 7.a shows K_{ext} measured over the 200-1000 nm wavelength range for OP2, OP9, OP17, OP27, OP32 and OP34. Under the fuel-lean conditions OP2 and OP9, K_{ext} exhibits a typical soot response with a maximum between 225 nm and 250 nm (Bescond et al. 2016; Schnaiter, M. et al. 2003) followed by a spectral decrease as a function of the wavelength above 400 nm as already seen in numerous studies (Bescond et al. 2016; Yon et al. 2011; Tregrossi et al. 2007; Schnaiter et al. 2003). Compared to OP2, under OP9 K_{ext} is higher since a higher number of aggregates with larger size are being produced. Looking into OP17 and above, an additional absorption signal with noticeable broad peaks were observed below 400 nm, indicating the presence of other absorbing species, most likely PAHs in the gas phase. This means that K_{ext} is resulting from 2 contributions: soot aggregates extinction ($K_{ext,soot}$), that accounts itself for both soot aggregates absorption ($K_{abs,soot}$) and soot aggregates total scattering ($K_{sca,soot}$) and the sum of all gas species absorption coefficients ($\sum_i K_{abs,i}$) (Eq.3).

$$K_{ext} = K_{abs,soot} + K_{sca,soot} + \sum_i K_{abs,i} \qquad \text{(Eq.3)}$$

As detailed further below (Eq.9), f_v is a function of $K_{abs,soot}$. Therefore, to calculate f_v from extinction measurements, $K_{sca,soot}$ and $\sum_i K_{abs,i}$ have to be estimated or removed from (Eq.3). $\sum_i K_{abs,i}$ is quantified by running a second set of measurements with a particle filter interposed between the sampling line and the light extinction cell: once all particles are removed, $K_{ext} \approx \sum_i K_{abs,i}$. Figure 7.b shows that $\sum_i K_{abs,i}$ increased with ϕ. It also clearly demonstrates that the gas phase absorbs only in the UV and that K_{ext} above 400 nm is solely due to soot aggregates. Furthermore, once the CS was used, K_{ext} displayed in Figure 7.c shows that the quasi-totality of the produced absorbing gas phase was oxidized bringing the extinction coefficients to the same shape (particularly in the UV) as OP2 or OP9 under untreated conditions.

[Figure 7 near here]

To identify the contribution of $K_{sca,soot}$, one needs information on both aggregates size distribution and morphology (see supplementary information S.4). Due to time and resource constraints, morphological parameters were evaluated only for 9 operating conditions that cover the burner's operating range as shown in Table 2. Consequently, $\overline{D_p}$ for the remaining OPs are interpolated with respect to ϕ (see supplementary information Figure S.3.7). For ease of use, $\overline{D_p}$ interpolation was performed with a second order polynomial function, which seemed to be the best trade-off between lower order fit error and higher order function overfitting. Meanwhile, for the rest of OPs for which D_f and k_f values were not determined, D_f and k_f were fixed at 1.851 and 1.970, respectively. These values correspond to the mean values of the D_f and k_f in Table 2 (all cases combined).

Using this information $K_{abs,soot} = K_{ext,soot} - K_{sca,soot} - \sum_i K_{abs,i}$ was obtained. Then $K_{abs,soot}$ was fitted with a power law of the form $\lambda^{-\alpha}$ between 400 nm and 1000 nm, with α the Ångström absorption exponent (Ångström 1929). Regardless of the exhaust condition (untreated or CS-treated), the fitting resulted in $\alpha > 1$ as summarized in Table 3. Considering only untreated conditions, α was found to vary from 1.32 ± 0.09 (under OP9) up to 2.06 ± 0.12 (under OP32).

[Table 3 near here]

Furthermore, α was evaluated from the fitting of $K_{abs,soot}$ between 400 nm and 1000 nm of all 34 OPs. Obtained α are available in supplementary information Table S.5.1. On average, in this study α was observed to increase with ϕ from 1.05 (under OP11) to 2.25 (under OP33). Compared to α evaluated for soot aggregates generated by propane miniCAST (Ess et al. 2021; Ess and Vasilatou 2019; Lefevre et al. 2018; Török et al. 2018; Kim et al. 2015; Schnaiter et al. 2006), much significant increase of α with ϕ was reported particularly by Kim et al. 2015 and Ess and Vasilatou 2019 with variation between 1.0 and 5.6. This dispersion may be due to differences in experimental conditions under which soot aggregates were obtained as much as it can be explained by how the power law fitting is performed and whether the total scattering has been accounted for. Despite all of that, α values obtained in this work are very well embedded in the domain covered by those previously reported in literature. Moreover, for soot aggregates generated by miniCAST using propane in a diffusion type flame Ess and Vasilatou 2019 have reported that α increased with the organic content of the aggregates. Similar observations have

also been reported by both Schnaiter et al. 2006 and Lefevre et al. 2018. The point that these studies made is that the more organic compounds the soot aggregates contain, the higher α is thus reflecting a sharp decrease in wavelength. In this regard, when the CS was used in the present study, α was observed to decrease for both fuel-lean and fuel-rich conditions hence varying between 1.10 and 1.66 (see supplementary information Table S.5.2). These findings suggest that PM obtained under these OPs exhibit different chemical compositions, responsible for such wavelength decrease. Investigating this aspect is beyond the scope of the article, and it will be investigated in a future work.

3.2.Comparative methods for the determination of the soot volume fraction

Over the years, many approaches have been reported to evaluate the soot volume fraction (f_v). These approaches are based either on a single analyzer or on a combination of different measurement methods and serve to compare different diagnostics and then indirectly to test the different assumptions made in aggregate and optical properties modeling. First, on the base of mobility size measurements, f_v is calculated comparing the spherical particles model with the model accounting for the aggregate's morphology. Then, f_v evaluated from mass concentration measurements and optical extinction coefficients are compared to the fractal aggregate approach using standard literature values for soot bulk density and optical properties.

3.2.1. Aggregate soot volume fraction vs. spherical model

In the most simplified approach, f_v can be evaluated by considering soot particles as agglomerates of polydisperse spheres. In this case, f_v is simply the sum over each class of size i of soot particle volume having a mobility-equivalent diameter $D_{m,i}$ and N_i number concentration of particles per unit volume of aerosol (Eq.4), therefore requiring only mobility-equivalent size distributions as provided by the SMPS measurements. This approach, referred to as "spherical approach" (or SMPS), oversimplifies the geometry of soot aggregates and thus is expected to overestimate f_v.

$$f_{v_{(SMPS)}} = \sum_{i}^{k} N_i \frac{\pi}{6} D_{m,i}^3 \qquad \text{(Eq.4)}$$

The second approach takes into account the fractal-like morphology of soot aggregates. This so-called "fractal-like aggregate approach" (or SMPS + STEM) accounts for morphological aspects by using the soot effective density ($\rho_{eff,i}$) which is size-dependent (Yon et al. 2015) and defined as the ratio of an aggregate mass and its volume based on its mobility-equivalent diameter (Baron et al. 2001). The aggregate mass may be written as a function of $\overline{D_p}$, N_p and soot bulk density (ρ_p), thus one may deduce the ratio (Eq.5) of $\rho_{eff,i}$ and ρ_p which is used to correct the first approach (Eq.4). In this case, soot particles are considered as polydisperse fractal-like aggregates (assuming monodisperse $D_{p,i} = \overline{D_p}$ and spherical primary particles size distribution). So, if an aggregate is a sphere, then $N_p = 1$ and $D_{m,i} = \overline{D_p}$.

$$\frac{\rho_{eff,i}}{\rho_p} = N_p \frac{\overline{D_p}^3}{D_{m,i}^3} \qquad \text{(Eq.5)}$$

Using the fractal law (Eq.2) describing aggregates morphology, the previous ratio can be then expressed as a function of measured quantities ($\overline{D_p}$, D_f, k_f and $D_{m,i}$). However, this requires converting the gyration diameter into a mobility-equivalent diameter. A simple conversion law, connecting the gyration diameter (D_g) and the electrical mobility diameter (D_m), of the form $\beta = D_g/D_m$ can be used (Rogak et al. 1993). In fact, the coefficient β depends on the flow regime (Wang and Sorensen 1999), which is characterized by Knudsen number (Kn). In the transient regime (i.e., $0.1 << Kn << 10$) which is the case here, β was found to fall in the range 1.03-1.35 (Kätzel et al. 2008; Gwaze et al. 2006; Sorensen 2001; Wang and Sorensen 1999; Rogak et al. 1993). Consequently, a conversion ratio of $\beta \sim 1.3$ is assumed, similarly to Yon et al. 2011 and Caumont-Prim et al. 2013. Combining (Eq.2) and (Eq.4) corrected with the density ratio (Eq.5), f_v can be formulated as in (Eq.6) while considering aggregates with $D_{m,i}$ smaller than $\overline{D_p}$ to be spherical, similarly to the approach proposed by Kelesidis and Pratsinis 2021.

$$f_{v_{(SMPS+STEM)}} = \begin{cases} \sum_{i}^{k} N_i \frac{\pi}{6} \beta^{D_f} k_f \overline{D_p}^{3-D_f} D_{m,i}^{D_f} & D_{m,i} > \overline{D_p} \\ \sum_{i}^{k} N_i \frac{\pi}{6} D_{m,i}^{3} & D_{m,i} \leq \overline{D_p} \end{cases} \quad \text{(Eq.6)}$$

Figure 8 compares the f_v calculated using the spherical and the fractal aggregate approaches. It is found that assuming all particles to be spherical overestimates on average by ~ 70 % the f_v compared to taking the morphology into consideration. This is globally the case for 9 data points (6 OPs of untreated and 3 of CS-treated exhaust) for which all parameters in (Eq.4) and (Eq.6) were measured except β. Adding the rest of the 34 OPs to the analysis (for both untreated and CS-treated exhaust), with assumed particle morphology, seems to corroborate the previous statement. Figure 8 also shows that this overestimation can reach up to a factor of 2.63 if an aggregate gyration and mobility-equivalent diameters were considered equivalent (i.e., β = 1.0). In a recent work, Kelesidis and Pratsinis 2021 showed that f_v derived from mobility data (neglecting aggregates fractal aspect) overestimated up to four times the f_v derived from mass-mobility measurements and that once the fractal-like morphology was accounted for this deviation decreased down to 6 %. In the light of this, we will consider that $f_{v_{(SMPS+STEM)}}$ calculated considering both mobility and morphological data as the reference f_v.

[Figure 8 near here]

3.2.2. Mass based vs. fractal aggregate volume fraction

Using filter deposition (see supplementary information Figure S.2.2), mass concentrations were measured. Table 3 summarizes the measured particulate mass concentrations (C_s) for both untreated and CS-treated exhaust. $f_{v_{(Mass)}}$ is obtained from (Eq.7) by assuming ρ_p:

$$f_{v_{(Mass)}} = \frac{C_s}{\rho_p} \quad \text{(Eq.7)}$$

Figure 9 shows $f_{v_{(Mass)}}$ for the selected OPs, assuming a value of ρ_p commonly found in the literature for mature soot ρ_p = 1800 kg/m^3 (Snelling et al. 2004; Choi et al. 1995). A roughly linear correlation with $f_{v_{(SMPS+STEM)}}$ is found. On average, using this approach seems to underestimate $f_{v_{(SMPS+STEM)}}$ except for untreated OP34 whose $f_{v_{(Mass)}}$ is overestimated. Modifying the bulk density assumption to ρ_p = 1296 kg/m^3 yields a slope of 1:1. This parameter tuning is in the range of previously reported ρ_p values for soot aggregates produced by a propane miniCAST that varied between 1227 kg/m^3 and 1543 kg/m^3 according to Yon et al. 2015.

[Figure 9 near here]

3.2.3. Volume fraction derived from extinction measurement

Optical extinction coefficients (K_{ext}) were measured between 200 nm and 1000 nm. It has been shown in section 3.1.3 that gas phase absorption contribution to K_{ext} is limited to below 400 nm. On the other hand, the average diameter of the primary particles ($\overline{D_p}$) were found to vary between 18 nm and ~ 39 nm. Considering $\overline{D_p}$ variation range, it was estimated that the soot total scattering accounts in the worst case for 6% at 700 nm (OP27). Since f_v was determined at 700 nm, the contribution of the scattering was neglected ($K_{ext} \approx K_{abs,soot}$). In this case, f_v could be evaluated using (Eq.9) if the soot absorption function E(m) is known. To a first approximation, a constant E(m, λ = 700 nm) = 0.35 was used (Simonsson et al. 2015).

$$f_{v_{(Optical)}} = \frac{\lambda K_{abs,soot}}{6\pi E(m,\lambda)} \qquad \text{(Eq.9)}$$

As shown in Figure 10, $f_{v_{(Optical)}}$ evaluated for all investigated cases is plotted against $f_{v_{(SMPS+STEM)}}$. Overall, $f_{v_{(Optical)}}$ shows a good agreement with $f_{v_{(SMPS+STEM)}}$ although it underestimated it by ~ 13 %. $f_{v_{(Optical)}}$ also agreed with $f_{v_{(Mass)}}$ although it overestimated it by ~ 25 % (not shown in the Figure). The main conclusion of this analysis is that despite the uncertainties inherent to each experimental method, f_v evaluated on the same samples with three methods based on completely different physical phenomena are in reasonable agreement.

4. Summary and conclusion

The exhaust of the diesel miniCAST was characterized over a wide range of operating conditions covering overall flame equivalence ratios from 0.103 to 1.645 using diesel B7 as fuel. The generated particulate matter (PM) was analyzed to describe its mobility-equivalent size distribution, morphology, mass concentration and optical extinction coefficient. The impact of adjusting the miniCAST flow rates demonstrated the ability of this burner to produce soot aggregates of variable size distributions and number concentrations offering a panel of choices for the targeted application. The burner was found to generate soot aggregates with geometric mean diameters (mobility diameters) in the range 45-105 nm with a geometric standard deviation in the range 1.5-1.8. Thanks to electron microscopy, key parameters describing the aggregates morphology were evaluated. The mean diameter of primary particles was found to increase from ~ 18 nm in fuel-lean conditions up to ~ 39 nm in fuel-rich conditions. The use of a catalytic stripper (CS) at 350 °C was found to alter soot aggregates size distributions that became more flattened. Soot aggregates PN losses within the CS were also evaluated and were found in good agreement with modeled losses accounting for diffusion and thermophoresis. The CS was not found to significantly alter soot aggregate morphology.

The miniCAST exhaust aerosol consisted not only of a particulate phase but also of a light absorbing gas phase whose contribution was significant to K_{ext} in the UV (< 400 nm) and that increased from fuel-lean to fuel-rich conditions. The Ångström absorption exponent (α) retrieved from optical absorption coefficients (accounting for total scattering contribution) between 400 nm and 1000 nm was found to increase from 1.05 under fuel-lean conditions up to 2.25 under fuel-rich conditions. Once the exhaust was thermally treated, the contributions to K_{ext} of absorbing species in the gas phase disappeared and the wavelength decrease in the visible and near-IR became less pronounced with α varying between 1.11 and 1.66. These observations, supported by TEM imaging suggest that the chemical composition of the exhaust, and most probably its organic content, play a significant role both on the shape and amplitude of K_{ext}.

Finally, a database with the following characteristics: PN, f_v, $D_{geo,m}$, σ_{geo,D_m}, $\overline{D_p}$, D_f and α was produced for the 34 operating points of the miniCAST including operating points without and with treatment (CS) of the exhaust. This database can be used by future users willing to

produce soot aggregates with specific characteristics. In addition, the procedure developed proved to be robust and reproducible and can be extended to new generation liquid fuels to test the influence of their chemical composition on the characteristics of the soot particles.

A second aspect of this work involved the evaluation of three independent measurement methods for determining the volume fraction of soot (f_v). These methods were based on the measurement of the aggregate size (combining mobility size distribution and morphology), the deposited mass and the optical extinction measurements. The main conclusions of this study are first that f_v evaluated on the basis of size mobility data alone overestimate by ~ 70 % the one accounting for morphological aspects (fractal aggregate approach), and second that f_v evaluated optically reasonably agreed with both f_v measured adopting the fractal aggregate approach (within 13 %) and f_v evaluated from mass concentration measurements (within 25 %) assuming a soot bulk density of 1800 kg/m^3. It turns out that the method based on optical extinction at 700 nm is a reliable and robust method. From this perspective and thanks to their simplicity, optical extinction-based sensors are worth exploring. Meanwhile, pressing technical issues of optics fouling and measurement sensitivity also have to be addressed to make this technology compliant with more restrictive tailpipe emission thresholds for modern engines supplied with any future liquid fuel.

Acknowledgments

The authors would like to acknowledge Dr. Virgile ROUCHON and Hedwige PONCET help in acquiring electron microscopy images and Jérôme CHEREL for the assistance in building the experimental setup.

Declaration of interest statement

The authors declare no competing interests.

References

Agudelo, J.R., Álvarez, A., and Armas, O. (2014). Impact of crude vegetable oils on the oxidation reactivity and nanostructure of diesel particulate matter. *Combust. Flame* 161 (11):2904–2915.

Ångström, A. (1929). On the Atmospheric Transmission of Sun Radiation and on Dust in the Air. *Geogr. Ann.* 11 (2):156–166.

Baron, P.A., Sorensen, C.M., and Brockmann, J.E. (2001). Nonspherical particle measurements: Shape factors, fractals, and fibers. *Aerosol Meas. Princ. Tech. Appl.* 705–749.

Bernstein, J.A., Alexis, N., Barnes, C., Bernstein, I.L., Nel, A., Peden, D., Diaz-Sanchez, D., Tarlo, S.M., and Williams, P.B. (2004). Health effects of air pollution. *J. Allergy Clin. Immunol.* 114 (5):1116–1123.

Bescond, A., Yon, J., Ouf, F.X., Ferry, D., Delhaye, D., Gaffié, D., Coppalle, A., and Rozé, C. (2014). Automated Determination of Aggregate Primary Particle Size Distribution by TEM Image Analysis: Application to Soot. *Aerosol Sci. Technol.* 48 (8):831–841.

Bescond, A., Yon, J., Ouf, F.-X., Rozé, C., Coppalle, A., Parent, P., Ferry, D., and Laffon, C. (2016). Soot optical properties determined by analyzing extinction spectra in the visible near-UV: Toward an optical speciation according to constituents and structure. *J. Aerosol Sci.* 101:118–132.

Bischof, O.F., Weber, P., Bundke, U., Petzold, A., and Kiendler-Scharr, A. (2020). Characterization of the Miniaturized Inverted Flame Burner as a Combustion Source to Generate a Nanoparticle Calibration Aerosol. *Emiss. Control Sci. Technol.* 6 (1):37–46.

Bond, T.C., Doherty, S.J., Fahey, D.W., Forster, P.M., Berntsen, T., DeAngelo, B.J., Flanner, M.G., Ghan, S., Kärcher, B., Koch, D., Kinne, S., Kondo, Y., Quinn, P.K., Sarofim, M.C., Schultz, M.G., Schulz, M., Venkataraman, C., Zhang, H., Zhang, S., Bellouin, N., Guttikunda, S.K., Hopke, P.K., Jacobson, M.Z., Kaiser, J.W., Klimont, Z., Lohmann, U., Schwarz, J.P., Shindell, D., Storelvmo, T., Warren, S.G., and Zender, C.S. (2013). Bounding the role of black carbon in the climate system: A scientific assessment. *J. Geophys. Res. Atmospheres* 118 (11):5380–5552.

Bourdrel, T., Bind, M.-A., Béjot, Y., Morel, O., and Argacha, J.-F. (2017). Cardiovascular effects of air pollution. *Arch. Cardiovasc. Dis.* 110 (11):634–642.

Cadrazco, M., Santamaría, A., and Agudelo, J.R. (2019). Chemical and nanostructural characteristics of the particulate matter produced by renewable diesel fuel in an automotive diesel engine. *Combust. Flame* 203:130–142.

Catalytic Instruments GmbH & Co.KG (2020). Application note CI-0009.

Caumont-Prim, C., Yon, J., Coppalle, A., Ouf, F.-X., and Ren, K.F. (2013). Measurement of aggregates' size distribution by angular light scattering. *J. Quant. Spectrosc. Radiat. Transf.* 126:140–149.

Choi, M.Y., Mulholland, G.W., Hamins, A., and Kashiwagi, T. (1995). Comparisons of the soot volume fraction using gravimetric and light extinction techniques. *Combust. Flame* 102 (1):161–169.

Durdina, L., Lobo, P., Trueblood, M.B., Black, E.A., Achterberg, S., Hagen, D.E., Brem, B.T., and Wang, J. (2016). Response of real-time black carbon mass instruments to mini-CAST soot. *Aerosol Sci. Technol.* 50 (9):906–918.

EN 590 (2022). Automotive fuels - Diesel - Requirements and test methods. CEN, Brussels.

Ess, M.N., Bertò, M., Irwin, M., Modini, R.L., Gysel-Beer, M., and Vasilatou, K. (2021). Optical and morphological properties of soot particles generated by the miniCAST 5201 BC generator. *Aerosol Sci. Technol.* 55 (7):828–847.

Ess, M.N. and Vasilatou, K. (2019). Characterization of a new miniCAST with diffusion flame and premixed flame options: Generation of particles with high EC content in the size range 30 nm to 200 nm. *Aerosol Sci. Technol.* 53 (1):29–44.

EU (2020). COMMISSION REGULATION (EU) 2018/1832 of 5 November 2018: amending Directive 2007/46/EC of the European Parliament and of the Council, Commission Regulation (EC) No 692/2008 and Commission Regulation (EU) 2017/1151 for the purpose of improving the emission type approval tests and procedures for light passenger and commercial vehicles, including those for in-service conformity and real-driving emissions and introducing devices for monitoring the consumption of fuel and electric energy.

Ghazi, R., Tjong, H., Soewono, A., Rogak, S.N., and Olfert, J.S. (2013). Mass, Mobility, Volatility, and Morphology of Soot Particles Generated by a McKenna and Inverted Burner. *Aerosol Sci. Technol.* 47 (4):395–405.

Gonzalez, A. (2020). Air quality in Europe - 2020 report (No. No 09/2020)*, EEA report*. Publications Office of the European Union, Luxembourg.
Greenberg, P.S. and Ku, J.C. (1997). Soot volume fraction imaging. *Appl Opt* 36 (22):5514–5522.
Grondin, D., Westermann, A., Breuil, P., Viricelle, J.P., and Vernoux, P. (2016). Influence of key parameters on the response of a resistive soot sensor. *Sens. Actuators B Chem.* 236:1036–1043.
Gwaze, P., Schmid, O., Annegarn, H.J., Andreae, M.O., Huth, J., and Helas, G. (2006). Comparison of three methods of fractal analysis applied to soot aggregates from wood combustion. *J. Aerosol Sci.* 37 (7):820–838.
IPCC (2022). Climate Change 2022: Impacts, Adaptation and Vulnerability. Contribution of Working Group II to the Sixth Assessment Report of the Intergovernmental Panel on Climate Change [H.-O. Pörtner, D.C. Roberts, M. Tignor, E.S. Poloczanska, K. Mintenbeck, A. Alegría, M. Craig, S. Langsdorf, S. Löschke, V. Möller, A. Okem, B. Rama (eds.)]. Cambridge University Press, Cambridge, UK and New York, NY, USA, 3056 pp.
Jacobson, M.Z. (2001). Strong radiative heating due to the mixing state of black carbon in atmospheric aerosols. *Nature* 409 (6821):695–697.
Kärcher, B. (2018). Formation and radiative forcing of contrail cirrus. *Nat. Commun.* 9 (1):1824.
Kätzel, U., Vorbau, M., Stintz, M., Gottschalk-Gaudig, T., and Barthel, H. (2008). Dynamic light scattering for the characterization of polydisperse fractal systems: II. Relation between structure and DLS results. *Part. Part. Syst. Charact.* 25 (1):19–30.
Kazemimanesh, M., Moallemi, A., Thomson, K., Smallwood, G., Lobo, P., and Olfert, J.S. (2019). A novel miniature inverted-flame burner for the generation of soot nanoparticles. *Aerosol Sci. Technol.* 53 (2):184–195.
Kelesidis, G.A. and Pratsinis, S.E. (2022). Santoro flame: The volume fraction of soot accounting for its morphology & composition. *Combust. Flame* 240:112025.
Kelesidis, G.A. and Pratsinis, S.E. (2021). Determination of the volume fraction of soot accounting for its composition and morphology. *Proc. Combust. Inst.* 38 (1):1189–1196.
Kim, J., Bauer, H., Dobovičnik, T., Hitzenberger, R., Lottin, D., Ferry, D., and Petzold, A. (2015). Assessing Optical Properties and Refractive Index of Combustion Aerosol Particles Through Combined Experimental and Modeling Studies. *Aerosol Sci. Technol.* 49 (5):340–350.
Kopnina, H. (2016). Vehicular air pollution and asthma: Implications for education for health and environmental sustainability. *Local Environ.* 22 (1):38–48.
Köylü, U.O., Faeth, G.M., Farias, T.L., and Carvalho, M.G. (1995). Fractal and projected structure properties of soot aggregates. *Combust. Flame* 100 (4):621–633.
Lapuerta, M., Ballesteros, R., and Martos, F.J. (2006). A method to determine the fractal dimension of diesel soot agglomerates. *J. Colloid Interface Sci.* 303 (1):149–158.
Lapuerta, M., Rodríguez–Fernández, J., and Sánchez-Valdepeñas, J. (2020). Soot reactivity analysis and implications on diesel filter regeneration. *Prog. Energy Combust. Sci.* 78:100833.
Lefevre, G., Yon, J., Liu, F., and Coppalle, A. (2018). Spectrally resolved light extinction enhancement of coated soot particles. *Atmos. Environ.* 186:89–101.
Li, Z., Song, C., Song, J., Lv, G., Dong, S., and Zhao, Z. (2011). Evolution of the nanostructure, fractal dimension and size of in-cylinder soot during diesel combustion process. *Combust. Flame* 158 (8):1624–1630.
Malmborg, V.B., Eriksson, A.C., Török, S., Zhang, Y., Kling, K., Martinsson, J., Fortner, E.C., Gren, L., Kook, S., Onasch, T.B., Bengtsson, P.-E., and Pagels, J. (2019). Relating aerosol mass spectra to composition and nanostructure of soot particles. *Carbon* 142:535–546.
Mamakos, A., Khalek, I., Giannelli, R., and Spears, M. (2013). Characterization of Combustion Aerosol Produced by a Mini-CAST and Treated in a Catalytic Stripper. *Aerosol Sci. Technol.* 47 (8):927–936.

Marhaba, I., Ferry, D., Laffon, C., Regier, T.Z., Ouf, F.-X., and Parent, P. (2019). Aircraft and MiniCAST soot at the nanoscale. *Combust. Flame* 204:278–289.
Migliorini, F., Thomson, K.A., and Smallwood, G.J. (2011). Investigation of optical properties of aging soot. *Appl. Phys. B* 104 (2):273–283.
Moallemi, A., Kazemimanesh, M., Corbin, J.C., Thomson, K., Smallwood, G., Olfert, J.S., and Lobo, P. (2019). Characterization of black carbon particles generated by a propane-fueled miniature inverted soot generator. *J. Aerosol Sci.* 135:46–57.
Moore, R.H., Ziemba, L.D., Dutcher, D., Beyersdorf, A.J., Chan, K., Crumeyrolle, S., Raymond, T.M., Thornhill, K.L., Winstead, E.L., and Anderson, B.E. (2014). Mapping the Operation of the Miniature Combustion Aerosol Standard (Mini-CAST) Soot Generator. *Aerosol Sci. Technol.* 48 (5):467–479.
Mueller, L., Schnelle-Kreis, J., Jakobi, G., Orasche, J., Jing, L., Canonaco, F., Prevot, A.S.H., and Zimmermann, R. (2016). Combustion process apportionment of carbonaceous particulate emission from a diesel fuel burner. *J. Aerosol Sci.* 100:61–72.
Ouf, F.X., Yon, J., Ausset, P., Coppalle, A., and Maillé, M. (2010). Influence of Sampling and Storage Protocol on Fractal Morphology of Soot Studied by Transmission Electron Microscopy. *Aerosol Sci. Technol.* 44 (11):1005–1017.
Pope III, C.A., Burnett, R.T., Thun, M.J., Calle, E.E., Krewski, D., Ito, K., and Thurston, G.D. (2002). Lung Cancer, Cardiopulmonary Mortality, and Long-term Exposure to Fine Particulate Air Pollution. *JAMA* 287 (9):1132–1141.
Popovicheva, O.B. and Starik, A.M. (2007). Aircraft-generated soot aerosols: Physicochemical properties and effects of emission into the atmosphere. *Izv. Atmospheric Ocean. Phys.* 43 (2):125–141.
Ranft, U., Schikowski, T., Sugiri, D., Krutmann, J., and Krämer, U. (2009). Long-term exposure to traffic-related particulate matter impairs cognitive function in the elderly. *Environ. Res.* 109 (8):1004–1011.
Rogak, S.N., Flagan, R.C., and Nguyen, H.V. (1993). The Mobility and Structure of Aerosol Agglomerates. *Aerosol Sci. Technol.* 18 (1):25–47.
Saffaripour, M., Tay, L.-L., Thomson, K.A., Smallwood, G.J., Brem, B.T., Durdina, L., and Johnson, M. (2017). Raman spectroscopy and TEM characterization of solid particulate matter emitted from soot generators and aircraft turbine engines. *Aerosol Sci. Technol.* 51 (4):518–531.
Santoro, R.J. and Miller, J.H. (1987). Soot particle formation in laminar diffusion flames. *Langmuir* 3 (2):244–254.
Santoro, R.J., Semerjian, H.G., and Dobbins, R.A. (1983). Soot particle measurements in diffusion flames. *Combust. Flame* 51:203–218.
Schnaiter, M., Gimmler, M., Llamas, I., Linke, C., Jäger, C., and Mutschke, H. (2006). Strong spectral dependence of light absorption by organic carbon particles formed by propane combustion. *Atmospheric Chem. Phys.* 6 (10):2981–2990.
Schnaiter, M., Horvath, H., Möhler, O., Naumann, K.-H., Saathoff, H., and Schöck, O.W. (2003). UV-VIS-NIR spectral optical properties of soot and soot-containing aerosols. *J. Aerosol Sci.* 34 (10):1421–1444. doi:10.1016/S0021-8502(03)00361-6.
Schumann, U. (2005). Formation, properties and climatic effects of contrails. *Comptes Rendus Phys.* 6 (4):549–565.
Seinfeld, J.H. (1998). Clouds, contrails and climate. *Nature* 391 (6670):837–838.
Simonsson, J., Olofsson, N.-E., Török, S., Bengtsson, P.-E., and Bladh, H. (2015). Wavelength dependence of extinction in sooting flat premixed flames in the visible and near-infrared regimes. *Appl. Phys. B* 119 (4):657–667.
Sipkens, T.A., Frei, M., Baldelli, A., Kirchen, P., Kruis, F.E., and Rogak, S.N. (2021). Characterizing soot in TEM images using a convolutional neural network. *Powder Technol.* 387:313–324.

Sipkens, T.A. and Rogak, S.N. (2021). Technical note: Using k-means to identify soot aggregates in transmission electron microscopy images. *J. Aerosol Sci.* 152:105699.
Snelling, D.R., Liu, F., Smallwood, G.J., and Gülder, Ö.L. (2004). Determination of the soot absorption function and thermal accommodation coefficient using low-fluence LII in a laminar coflow ethylene diffusion flame. *Combust. Flame* 136 (1):180–190.
Sorensen, C.M. (2001). Light Scattering by Fractal Aggregates: A Review. *Aerosol Sci. Technol.* 35 (2):648–687.
Sorensen, C.M. and Roberts, G.C. (1997). The Prefactor of Fractal Aggregates. *J. Colloid Interface Sci.* 186 (2):447–452.
Soriano, J.A., Agudelo, J.R., López, A.F., and Armas, O. (2017). Oxidation reactivity and nanostructural characterization of the soot coming from farnesane - A novel diesel fuel derived from sugar cane. *Carbon* 125:516–529.
Swinehart, D.F. (1962). The Beer-Lambert Law. *J. Chem. Educ.* 39 (7):333.
Török, S., Malmborg, V.B., Simonsson, J., Eriksson, A., Martinsson, J., Mannazhi, M., Pagels, J., and Bengtsson, P.-E. (2018). Investigation of the absorption Ångström exponent and its relation to physicochemical properties for mini-CAST soot. *Aerosol Sci. Technol.* 52 (7):757–767.
Tregrossi, A., Barbella, R., Ciajolo, A., and Alfè, M. (2007). Spectral properties of soot in the uv-visible range. *Combust. Sci. Technol.* 179 (1–2):371–385.
U.S. Energy Information Administration (2021). International energy outlook 2021 with projections to 2050.
Wang, G.M. and Sorensen, C.M. (1999). Diffusive mobility of fractal aggregates over the entire knudsen number range. *Phys Rev E* 60 (3):3036–3044.
Ye, P., Sun, C., Lapuerta, M., Agudelo, J., Wal, R.V., Boehman, A.L., Toops, T.J., and Daw, S. (2016). Impact of rail pressure and biodiesel fueling on the particulate morphology and soot nanostructures from a common-rail turbocharged direct injection diesel engine. *Int. J. Engine Res.* 17 (2):193–208.
Yon, J., Bescond, A., and Ouf, F.-X. (2015). A simple semi-empirical model for effective density measurements of fractal aggregates. *J. Aerosol Sci.* 87:28–37.
Yon, J., Lemaire, R., Therssen, E., Desgroux, P., Coppalle, A., and Ren, K.F. (2011). Examination of wavelength dependent soot optical properties of diesel and diesel/rapeseed methyl ester mixture by extinction spectra analysis and LII measurements. *Appl. Phys. B* 104 (2):253–271.

Table caption

Table 1. Settings of operating points of the liquid fuel miniCAST burner and resulting flame overall equivalence ratios (ϕ).

Table 2**.** Morphological properties of soot aggregates resulting from STEM images analysis. $D_{geo,p}$ and σ_{geo,D_p} uncertainties correspond to the 95 % confidence interval of the sigmoid law (Eq.S.3.3) fit.

Table 3. Ångström absorption exponent (α) evaluated by fitting $K_{abs,soot}$ using a power law of the form $\lambda^{-\alpha}$ between 400 nm and 1000 nm. Uncertainties correspond to day-to-day variations and PM mass concentration (C_s) for miniCAST OPs for untreated and CS-treated exhaust. Data not corrected for dilution (~ 19:1).

Figure caption

Figure 1. Schematic of the experimental exhaust bench and aerosol characterization setup.

Figure 2. Descriptive schematic of the miniCAST burner model 5102 D (Jing Ltd., Switzerland) for liquid fuels. The indicated parameters are used to change soot properties.

Figure 3. SMPS measured aggregate number concentration (PN), mobility-equivalent geometric mean diameter ($D_{geo,m}$) and geometric standard deviation (σ_{geo,D_m}) as function of flame overall equivalence ratio (ϕ) for 34 OPs for untreated exhaust using diesel B7. OP2, OP9, OP17, OP27, OP32 and OP34 are indicated in colors. (a, b, c) oxidation air = 2 L/min and (d, e, f) mixing air = 0.1 L/min. Uncertainties account for 3 size distributions measured consecutively. Data not corrected for dilution (~ 19:1).

Figure 4. Soot aggregates mobility-equivalent size distributions obtained under OP2, OP9, OP17, OP27, OP32 and OP34 for (a) untreated exhaust and (b) CS-treated exhaust using diesel B7. Each size distribution is the average of 3 consecutive size distributions. Data not corrected for dilution (~ 19:1). Statistical descriptors of these size distributions are made available in supplementary information Table S.2.1.

Figure 5. Fitting measured soot aggregates mobility-equivalent size distributions obtained under (a) OP27 and (b) OP34 for untreated exhaust, with either monomodal or bimodal log-normal PDFs and extrapolating truncated data from 224.7 nm to 400 nm. Data not corrected for dilution (~ 19:1).

Figure 6. Scanning transmission electron microscopy (STEM) (left row) and transmission electron microscopy (TEM) (right row) images of representative miniCAST soot aggregates for untreated exhaust obtained under (a) OP2, (b) OP9, (c) OP17, (d) OP27, (e) OP32 and (f) OP34.

Figure 7. Optical extinction coefficients (K_{ext}) measured under OP2, OP9, OP17, OP27, OP32 and OP34 for (a) untreated (raw) exhaust, (b) filtered exhaust and (c) thermally treated (CS-treated) exhaust.

Figure 8. $f_{v_{(SMPS)}}$ evaluated assuming polydisperse spherical particles vs. $f_{v_{(SMPS+STEM)}}$ calculated assuming polydisperse fractal-like aggregates. Data not corrected for dilution (~ 19:1).

Figure 9. $f_{v_{(Mass)}}$ evaluated from soot deposits assuming a constant soot bulk density (ρ_p = 1800 kg/m^3) vs. $f_{v_{(SMPS+STEM)}}$ assuming polydisperse fractal-like aggregates. Data not corrected for dilution (~ 19:1).

Figure 10. $f_{v_{(Optical)}}$ calculated assuming a constant absorption function (E(m) = 0.35) at 700 nm vs. $f_{v_{(SMPS+STEM)}}$. Data not corrected for dilution (~ 19:1).

Table 1. Settings of operating points of the liquid fuel miniCAST burner and resulting flame overall equivalence ratios (ϕ).

Operating point (OP)	**Liquid fuel flow rate [µL/min]**	**Mixing air flow rate [mL/min]**	**Oxidation air flow rate [L/min]**	**Internal dilution air flow rate [L/min]**	**Flame overall equivalence ratio (ϕ) (diesel B7)**
OP2	50	100	3	20	0.103
OP9	50	100	2	20	0.291
OP17	100	10	2	20	0.616
OP27	250	100	3	20	0.913
OP32	250	100	2	20	1.457
OP34	250	10	2	20	1.539

Table 2**.** Morphological properties of soot aggregates resulting from STEM images analysis. $D_{geo,p}$ and σ_{geo,D_p} uncertainties correspond to the 95 % confidence interval of the sigmoid law (Eq.S.3.3) fit.

Operating point (OP)	**Condition**	**Number of analyzed aggregates**	**Estimated error on aggregate area [%]**	$\mathbf{D_{geo,p}}$ **[nm]**	$\boldsymbol{\sigma_{geo,D_p}}$	$\mathbf{D_f}$	$\mathbf{k_f}$
OP2	Untreated	139	±10	22.3 ± 0.4	1.518 ± 0.012	1.839	1.967
OP9	Untreated	198	± 11	18.0 ± 0.4	1.580 ± 0.015	1.805	1.960
OP17	Untreated	156	± 7	34.4 ± 0.3	1.497 ± 0.007	1.941	1.988
OP27	Untreated	179	± 8	35.2 ± 0.2	1.431 ± 0.004	1.831	1.966
OP32	Untreated	138	± 8	34.4 ± 0.4	1.425 ± 0.007	1.862	1.972
OP34	Untreated	164	± 7	39.2 ± 0.2	1.394 ± 0.003	1.844	1.968
OP9	CS-treated	141	± 9	19.7 ± 0.3	1.567 ± 0.013	1.849	1.970
OP27	CS-treated	229	± 8	34.5 ± 0.3	1.377 ± 0.005	1.790	1.957
OP34	CS-treated	164	± 9	35.2 ± 0.3	1.394 ± 0.005	1.834	1.966

Table 3. Ångström absorption exponent (α) evaluated by fitting $K_{abs,soot}$ using a power law of the form $\lambda^{-\alpha}$ between 400 nm and 1000 nm. Uncertainties correspond to day-to-day variations and PM mass concentration (C_s) for miniCAST OPs for untreated and CS-treated exhaust. Data not corrected for dilution (~ 19:1).

Operating point (OP)	**Ångström absorption exponent (α)**		**Mass concentration C_s [mg/m^3]**	
	Untreated	**CS-treated**	**Untreated**	**CS-treated**
OP2	1.42 ± 0.04	-	0.80	0.73
OP9	1.32 ± 0.09	1.26 ± 0.15	4.00	2.73
OP17	1.72 ± 0.20	1.44 ± 0.03	9.53	6.20
OP27	1.68 ± 0.03	1.22 ± 0.05	18.07	11.67
OP32	2.06 ± 0.12	1.27 ± 0.10	7.67	3.00
OP34	2.01 ± 0.17	1.45 ± 0.21	15.27	4.07

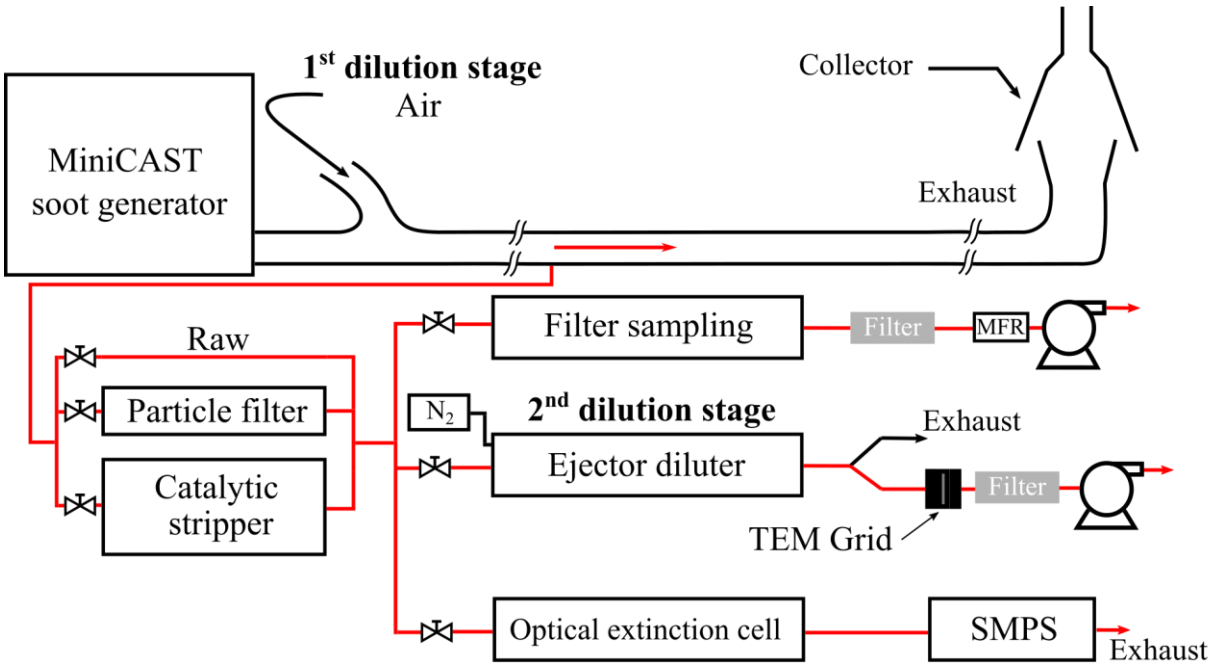

Figure 1. Schematic of the experimental exhaust bench and aerosol characterization setup.

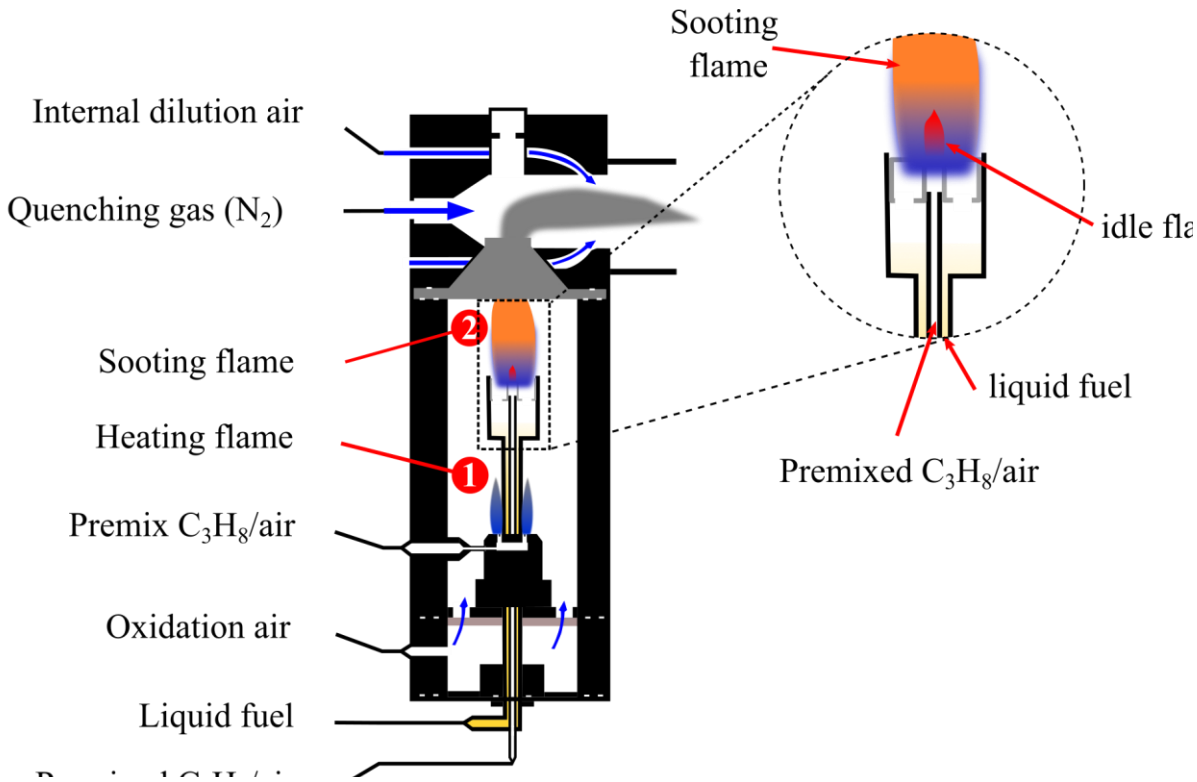

Figure 2. Descriptive schematic of the miniCAST burner model 5102 D (Jing Ltd., Switzerland) for liquid fuels. The indicated parameters are used to change soot properties.

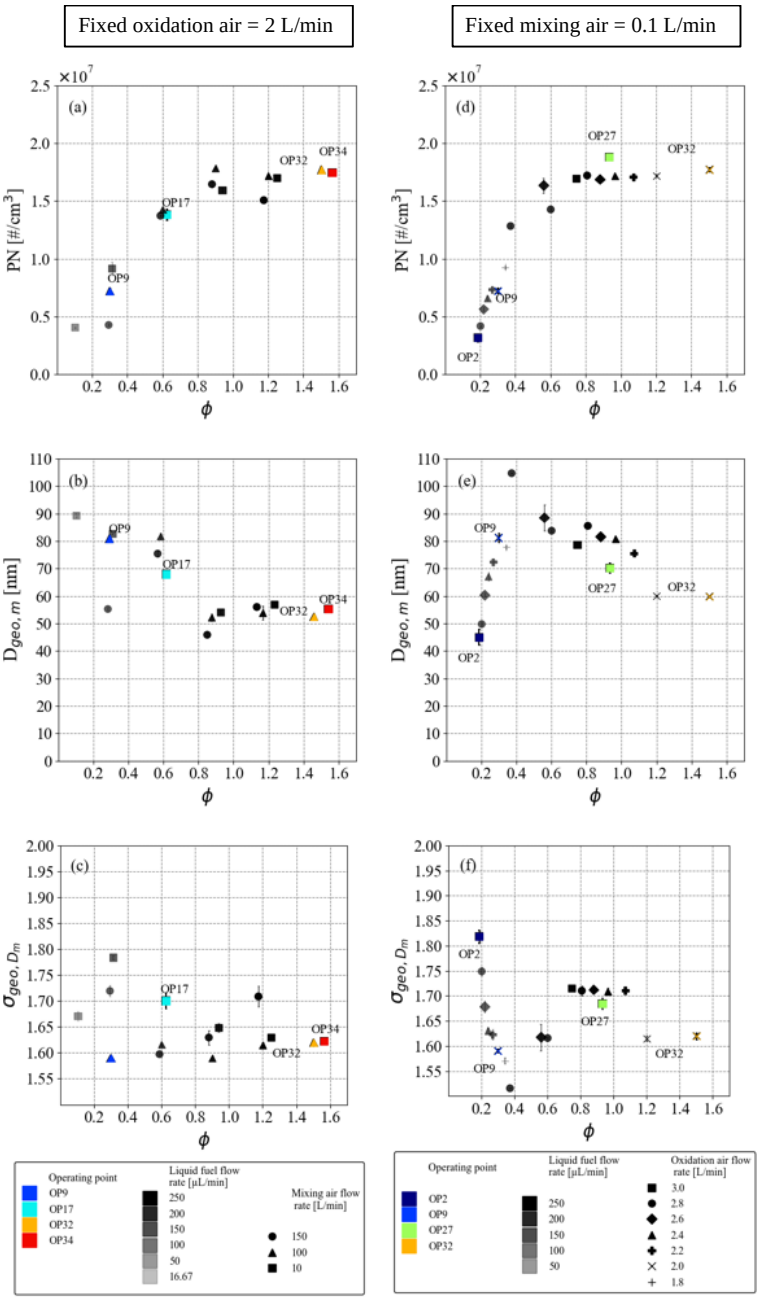

Figure 3. SMPS measured aggregate number concentration (PN), mobility-equivalent geometric mean diameter ($D_{geo,m}$) and geometric standard deviation (σ_{geo,D_m}) as function of flame overall equivalence ratio (ϕ) for 34 OPs for untreated exhaust using diesel B7. OP2, OP9, OP17, OP27, OP32 and OP34 are indicated in colors. (a, b, c) oxidation air = 2 L/min and (d, e, f) mixing air = 0.1 L/min. Uncertainties account for 3 size distributions measured consecutively. Data not corrected for dilution (~ 19:1).

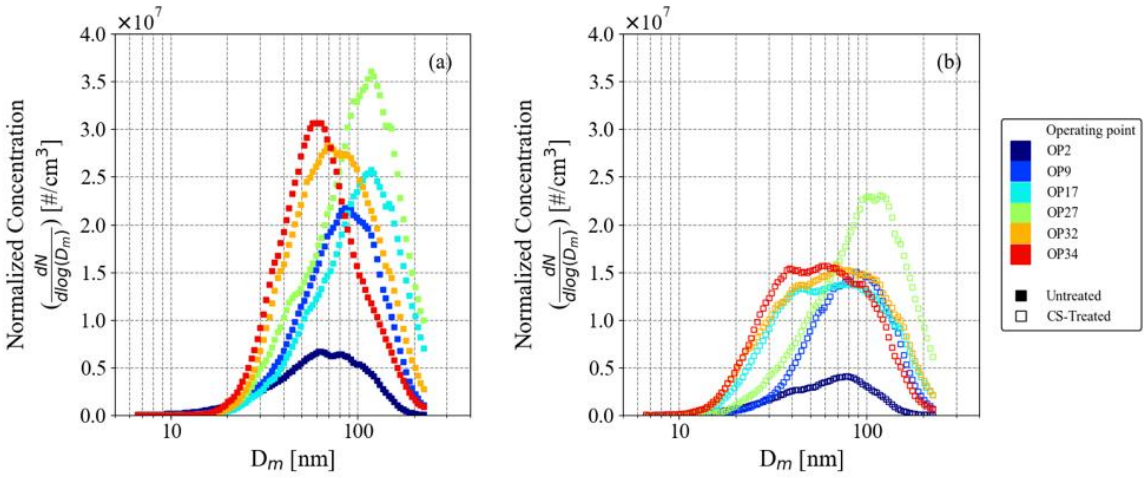

Figure 4. Soot aggregates mobility-equivalent size distributions obtained under OP2, OP9, OP17, OP27, OP32 and OP34 for (a) untreated exhaust and (b) CS-treated exhaust using diesel B7. Each size distribution is the average of 3 consecutive size distributions. Data not corrected for dilution (~ 19:1). Statistical descriptors of these size distributions are made available in supplementary information Table S.2.1.

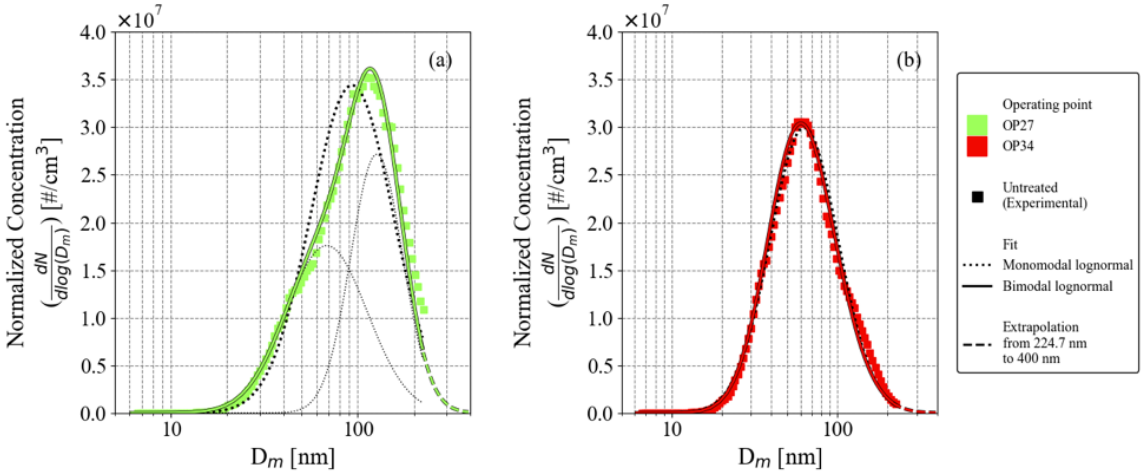

Figure 5. Fitting measured soot aggregates mobility-equivalent size distributions obtained under (a) OP27 and (b) OP34 for untreated exhaust, with either monomodal or bimodal log-normal PDFs and extrapolating truncated data from 224.7 nm to 400 nm. Data not corrected for dilution (~ 19:1).

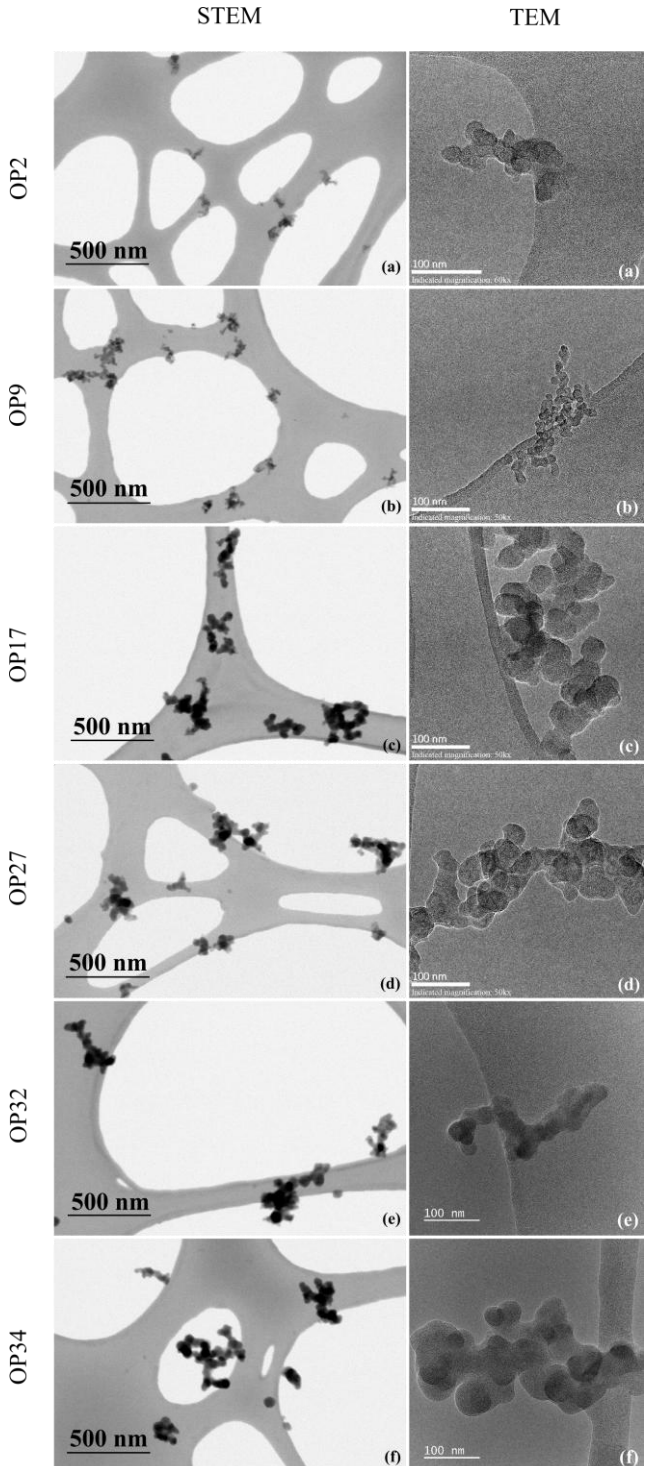

Figure 6. Scanning transmission electron microscopy (STEM) (left row) and transmission electron microscopy (TEM) (right row) images of representative miniCAST soot aggregates for untreated exhaust obtained under (a) OP2, (b) OP9, (c) OP17, (d) OP27, (e) OP32 and (f)

OP34.

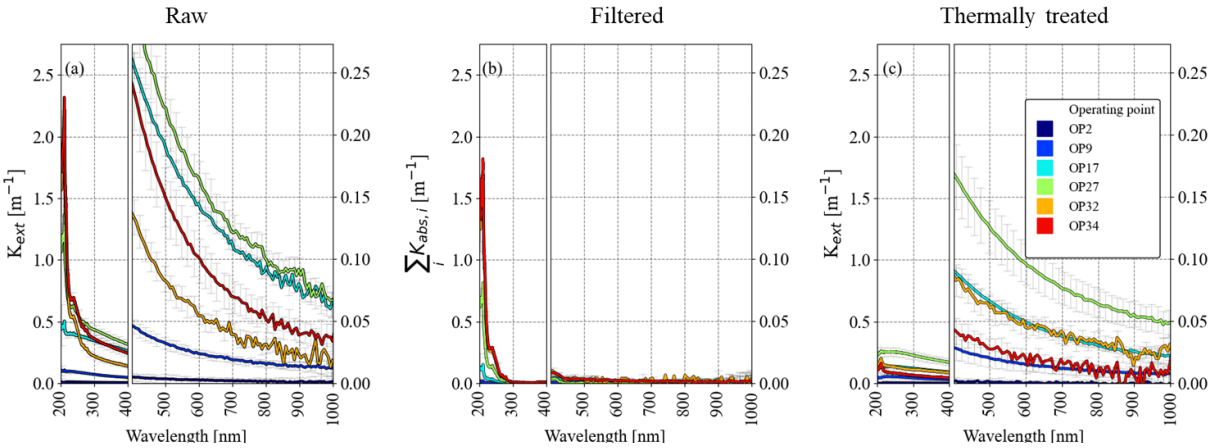

Figure 7. Optical extinction coefficients (K_{ext}) measured under OP2, OP9, OP17, OP27, OP32 and OP34 for (a) untreated (raw) exhaust, (b) filtered exhaust and (c) thermally treated (CS-treated) exhaust.

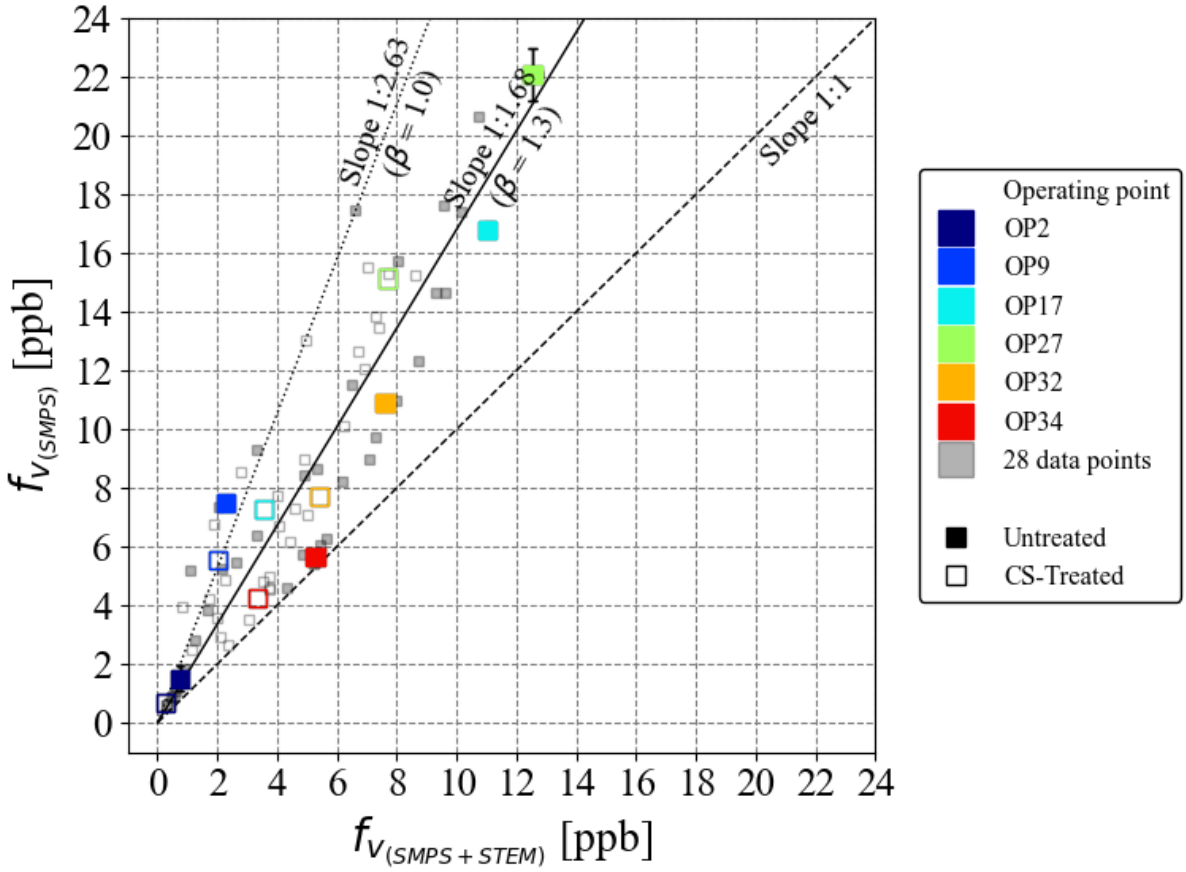

Figure 8. $f_{V(SMPS)}$ evaluated assuming polydisperse spherical particles vs. $f_{V(SMPS+STEM)}$ calculated assuming polydisperse fractal-like aggregates. Data not corrected for dilution (~ 19:1).

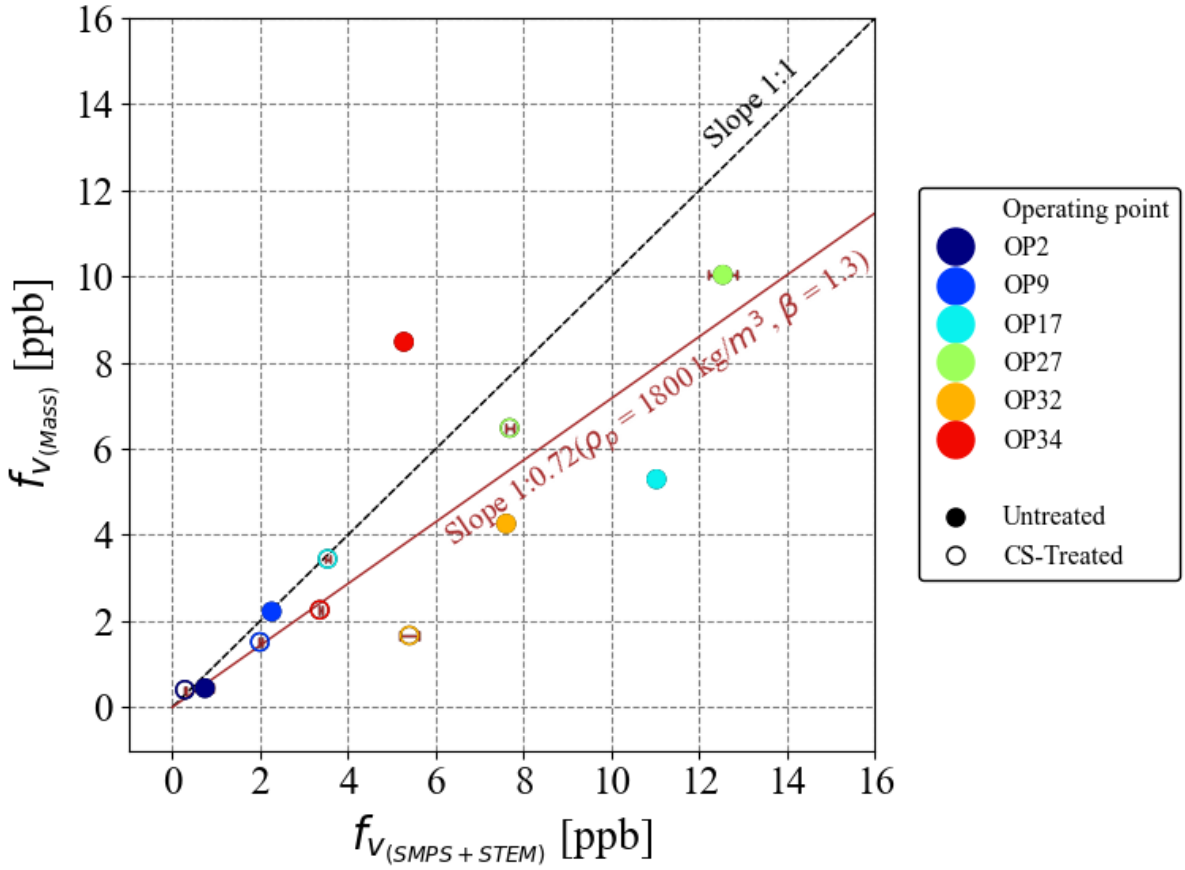

Figure 9. $f_{V(Mass)}$ evaluated from soot deposits assuming a constant soot bulk density (ρ_p = 1800 kg/m^3) vs. $f_{V(SMPS+STEM)}$ assuming polydisperse fractal-like aggregates. Data not corrected for dilution (~ 19:1).

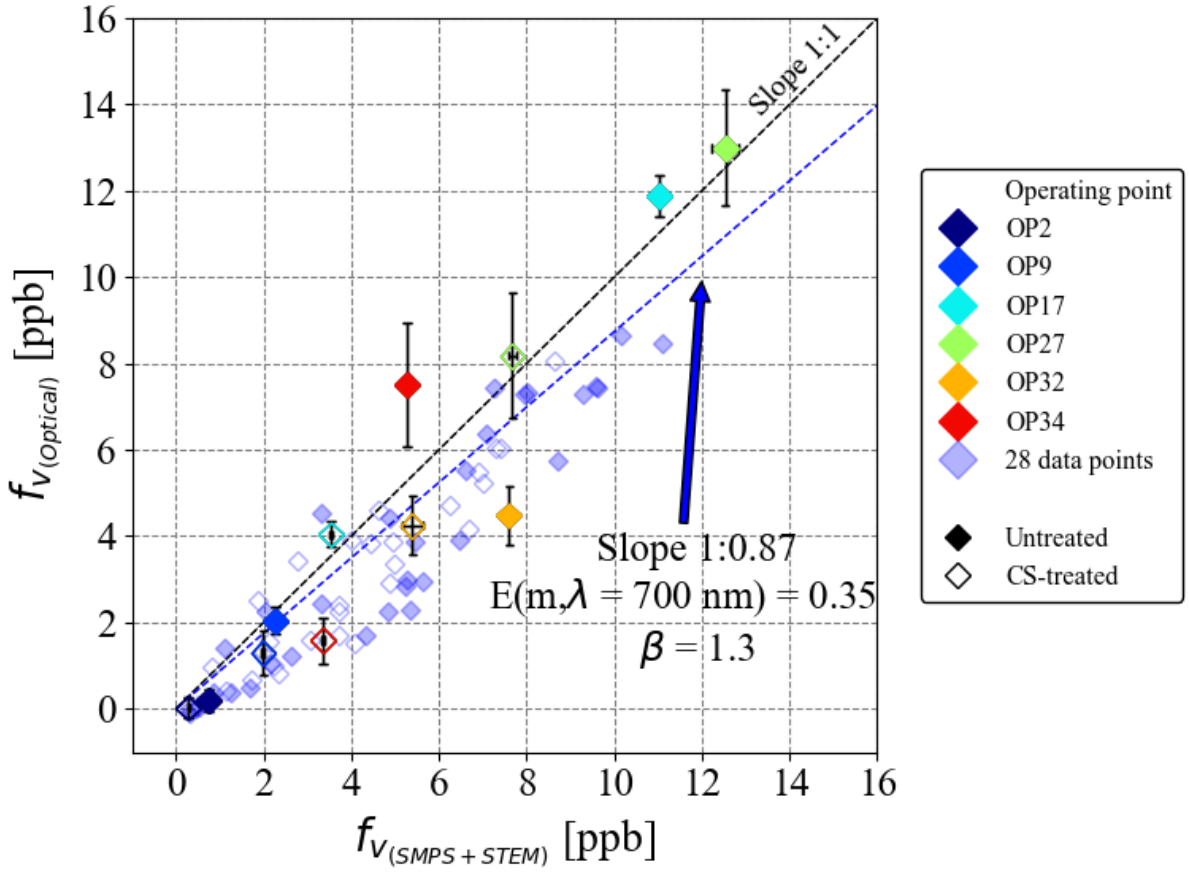

Figure 10. $f_{V(Optical)}$ calculated assuming a constant absorption function (E(m) = 0.35) at 700 nm vs. $f_{V(SMPS+STEM)}$. Data not corrected for dilution (~ 19:1).

Supplementary Information:

Comprehensive characterization of particulate matter emission

produced by a liquid-fueled miniCAST burner

Mouad Daoudi [a,b], Philipp Schiffmann [a], Alessandro Faccinetto [b], Arnaud Frobert [a], Pascale Desgroux [b]

[a] IFP Energies Nouvelles, Institut Carnot IFPEN TE, France

[b] Univ. Lille, CNRS, UMR 8522 - PC2A - Physicochimie des Processus de Combustion et de l'Atmosphère, Lille F-59000, France

Corresponding author: pascale.desgroux@univ-lille.fr

5. Content

S.1.MiniCAST operating conditions, soot production stability and repeatability
- ***Chemical composition of diesel B7 and some of its properties***
- ***Operating points***
- ***Sampling conditions***
- ***MiniCAST stability over time***
- ***Soot production repeatability***

S.2.Size distributions and deposit on filters
- ***Impact of miniCAST flow rates for CS-treated exhaust***
- ***Soot aggregates size distributions statistical descriptors***
- ***Deposits on filters***

S.3.Electron microscopy diagnostic
- ***Sampling conditions***
- ***STEM images analysis***
  - *Segmentation process*
  - *EDM-SBS process*
  - *Normalized mean EDM-SBS function interpretation*
  - *Fractal analysis*
- ***Impact of the catalytic stripper***
- ***Mean primary particle diameters***

S.4.Gas phase and total scattering contribution to extinction

S.5.Overview of operating points characteristics

6. S.1.MiniCAST operating conditions, soot production stability and repeatability

7. Chemical composition of diesel B7 and some of its properties

Table.R.1 Chemical composition of liquid diesel B7 and some of its properties.

Average chemical Formula	$C_{14.5}H_{26.7}O_{0.1}$
Density at T = 15 °C (kg/m³)	831.5
Air-fuel ratio (stoichiometric)	14.37
Centane number	48.2
GCxGC-FID analysis of the chemical composition of liquid diesel B7 (wt. %)	
Iso-paraffins	27.4
Normal-paraffins	7.7
Mononaphthenes	19.4
Di-naphthenes	12.5
Di-aromatics	16.4
Naphenic-di-aromatics	6.9
Monoaromatics	2.7
Naphenic-monoaromatics	1.5
Tri-aromatics	0.3
Tetra-aromatics	0.1
Methyl esters	5.1

Operating points

8. Table S.1.1. Settings of operating points (OPs) of the liquid fuel miniCAST burner and resulting flame overall equivalence ratio ($\boldsymbol{\phi}$). OPs in bold are those for which all diagnostics presented in the main text were performed.

Operating point (OP)	**Liquid fuel flow rate [µL/min]**	**Mixing air flow rate [mL/min]**	**Oxidation air flow rate [L/min]**	**Internal dilution air flow rate [L/min]**	**Flame overall equivalence ratio diesel B7** (ϕ)
OP1	16.67	10	2	20	0.103
OP2	**50**	**100**	**3**	**20**	**0.183**
OP3	50	50	3	20	0.189
OP4	50	100	2.8	20	0.197
OP5	50	100	2.6	20	0.215
OP6	50	100	2.4	20	0.235
OP7	50	100	2.2	20	0.260
OP8	50	150	2	20	0.283
OP9	**50**	**100**	**2**	**20**	**0.291**
OP10	50	10	2	20	0.308
OP11	50	100	1.8	20	0.331
OP12	50	10	1.6	20	0.411
OP13	100	100	3	20	0.365

OP14	100	150	2	20	0.566
OP15	100	100	2	20	0.583
OP16	150	100	3	20	0.548
OP17	**100**	**10**	**2**	**20**	**0.616**
OP18	200	150	3	20	0.717
OP19	200	100	3	20	0.730
OP20	200	10	3	20	0.756
OP21	200	100	2.8	20	0.789
OP22	150	150	2	20	0.849
OP23	150	100	2	20	0.874
OP24	200	100	2.6	20	0.859
OP25	150	10	2	20	0.923
OP26	200	100	2.4	20	0.941
OP27	**250**	**100**	**3**	**20**	**0.913**
OP28	200	100	2.2	20	1.041
OP29	200	150	2	20	1.132
OP30	200	100	2	20	1.165
OP31	200	10	2	20	1.231
OP32	**250**	**100**	**2**	**20**	**1.457**
OP33	200	10	1.6	20	1.645
OP34	**250**	**10**	**2**	**20**	**1.539**

9.

Sampling conditions

The miniCAST exhaust was diluted using either one external dilution stage or two external dilutions stages, the use of which may alter soot aggregates size distribution properties through coagulation and agglomeration processes within the sampling line. Exhaust dilution is mainly performed to lower soot aggregates concentrations, so it does not saturate measuring instruments such as SMPS. Figure S.1.1 describes soot aggregates size distribution parameters (PN, $D_{geo,m}$ and f_v) measured by the SMPS for untreated exhaust obtained under OP9 as a function of the global dilution ratio (volumetric). Each sub-figure shows, two data sets. The first data set with global dilution ratios < 30 corresponds to the case where only the first external dilution stage was varied, while the rest of the data points corresponds to the case where both the first and second external dilutions stages were used. It is worth reminding that the second external dilution stage imposes a fixed dilution ratio (~ 11: 1) and that for both data sets variation in the global dilution ratio was obtained by varying the amount of added air using the first external dilution stage.

Looking into Figure S.1.1.a, one can see that PN decreased almost proportionally to the imposed global dilution ratio, using either the first dilution stage or both the first and second dilution stages. But a slight deviation from the slope (-1) is observed at low dilution ratio. Figure S.1.1.b shows that increasing the global dilution ratio by a factor of ~ 10 resulted in shifting OP9's $D_{geo,m}$ towards the lower size by ~ 9.4 nm (-12 %). However, the shape of the size distribution (not shown) remained unaffected. Figure S.1.1.c shows that the soot volume fraction $f_{v_{(SMPS+STEM)}}$ evolution with dilution ratio follows the expected slope (-1) for the same dataset as Figure. S.1.1.a. As a result, the choice was made to carry out all experiments at the same global dilution ratio of ~ 19:1. If soot aggregates coagulation along the sampling line occurs, this is not a problem as long as all diagnostics are performed at approximately the same location downstream the sampling line.

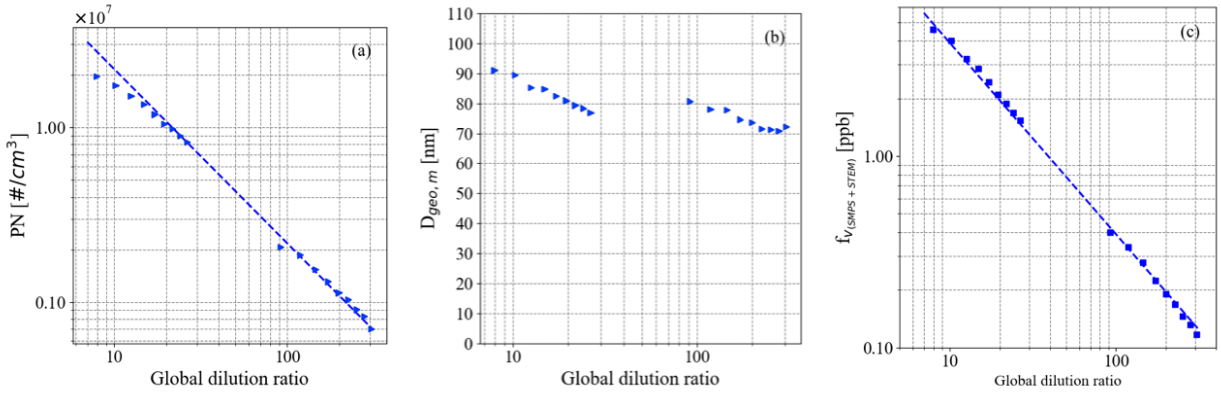

Figure S.1.1**.** Impact of dilution on soot aggregates (a) number concentration (PN) and (b) mobility-equivalent geometric mean diameter ($D_{geo,m}$) and (c) soot volume fraction $f_{v_{(SMPS+STEM)}}$ calculated assuming polydisperse fractal-like aggregates for untreated exhaust obtained under OP9.

MiniCAST stability over time

Conducting experiments on a soot containing exhaust requires that properties of soot aggregates size distribution (PN, $D_{geo,m}$ and σ_{geo,D_m}) generated under a given condition remains stable for extended time periods. This is very important if such soot generator must be used as reference for calibrating other instruments. After integrating the soot

generator into the experimental setup, improving the control of mass flow controllers and the burner stability, the miniCAST was operated over 6 months for both short (< 20 minutes) and long (up to 90 minutes) periods of time. Soot production stability was monitored using, a Pegasor particle sensor, type M (PPS-M, Pegasor, Oy) (not shown) that was in fact installed after the first external dilution stage and before preparing exhaust for diagnostics as shown previously in Figure 1. Raw exhaust was routed to the PPS-M inlet by means of a wall heater maintained at 180 °C and the sensor body was maintained at 250 °C. Soot PN was found to be rather stable within 10 % coefficient of variation (i.e., coefficient of variation (x) = mean(x)/std(x)) of soot PN for most experiments and across the tested OPs, except OP2 where this coefficient was found to be close to 20 % as shown in Figure S.1.2. Soot PN was slightly less stable (coefficient of variation increased to ~ 20 %) in June 2021 when the soot generator showed signs of clogging issues. After being cleaned soot production stability returned to the level described before.

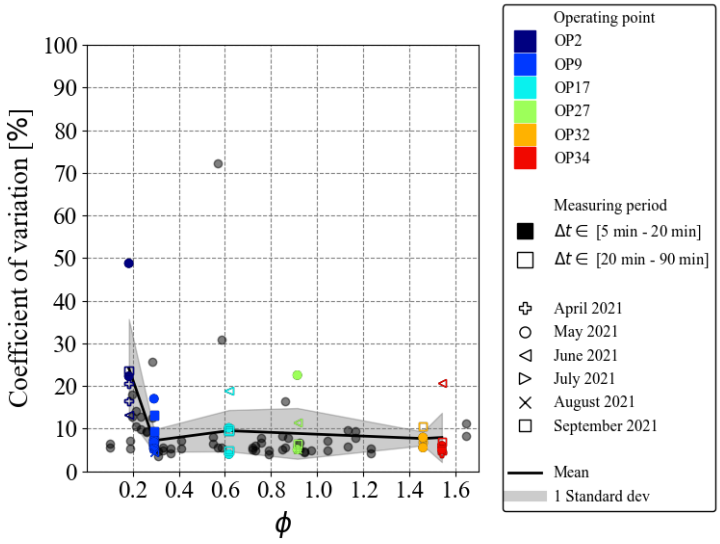

Figure S.1.2. Coefficient of variation of soot PN (coefficient of variation (x) = mean(x)/std(x)). PN was estimated using PPS-M.

Soot production repeatability

The measurement of soot aggregates PN, $D_{geo,m}$ and σ_{geo,D_m} (for OP2, OP9, OP17, OP27, OP32 and OP34) over 5 months testing period showed that soot production remained

stable. To minimize possible variations with time, the choice was made to consider the fuel-lean condition OP9 as a reference condition to be tested each time the burner was used. Any significant drift from OP9's $D_{geo,m}$ triggered a cleaning procedure of the burner. As a result, PN, $D_{geo,m}$ and σ_{geo,D_m} varied at worse of 30 % (e.g., OP2), 17 % (e.g., OP2) and 5 % (e.g., OP2), and at best of 4 % (e.g., OP27), 7 % (e.g., OP34) and 0.5 % (e.g., OP34), respectively (see Figure S.1.3). Overall, these variations are in line with the propane miniCAST for which PN varied by a factor of 2 over a similar evaluation period (Moore et al. 2014). Indeed, several factors can contribute to such variations, for instance soot accumulation in the sampling lines or valves or clogging issues inside the burner due to its heating system which tends to cause coking on the inside of the burner tube.

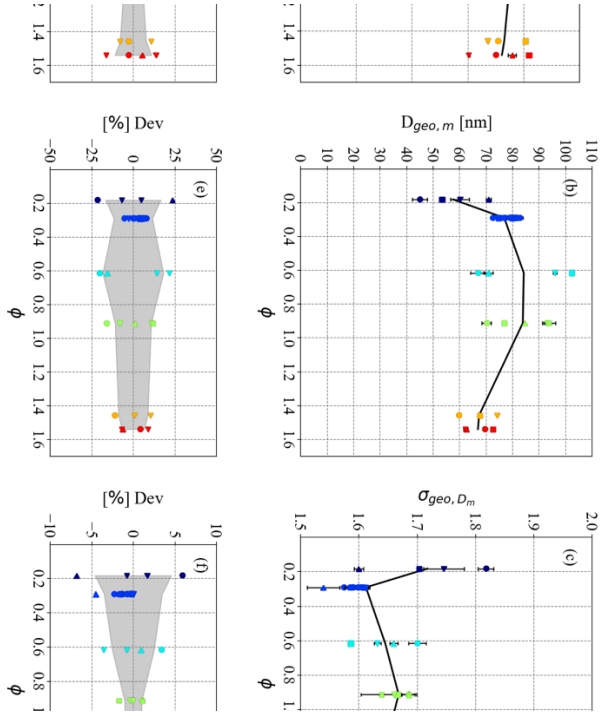

Figure S.1.3. (a, b, c): SMPS measured aggregates number concentration (PN), mobility-equivalent geometric mean diameter ($D_{geo,m}$) and geometric standard deviation (σ_{geo,D_m}) as function of flame overall equivalence ratio (ϕ) for OP2, OP9, OP17, OP27, OP32 and OP34 operating points over time for untreated exhaust using diesel B7. (d, e, f) Their respective deviations to the mean curve accounts for repeatability over 5 months.

Uncertainties account for 3 size distributions measured consecutively. Data not corrected for dilution (~ 19:1).

10. S.2.Size distributions and deposit on filters

Impact of miniCAST flow rates for CS-treated exhaust

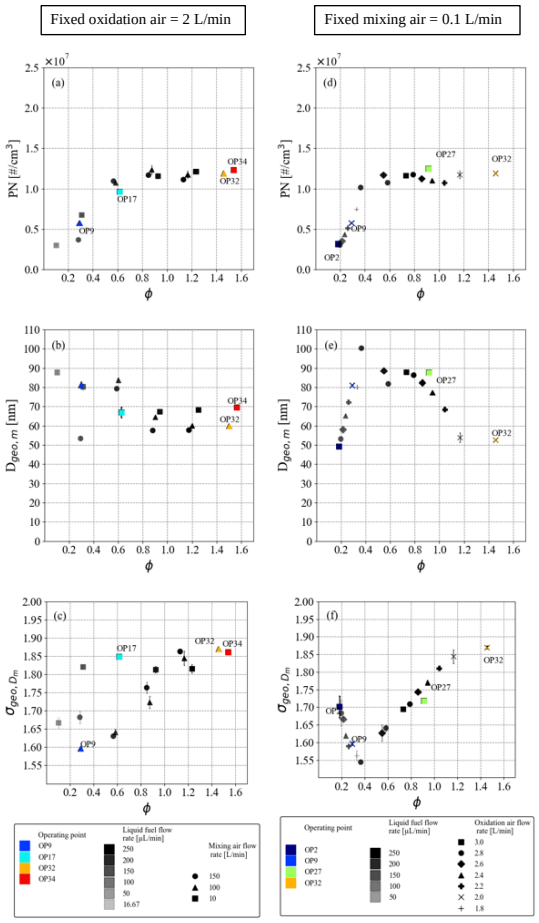

Figure S.2.1. SMPS measured aggregates number (PN), mobility-equivalent geometric mean diameter ($D_{geo,m}$) and geometric standard deviation (σ_{geo,D_m}) as function of flame overall equivalence ratio (ϕ) for 34 OPs for CS-treated exhaust using diesel B7. OP2, OP9, OP17, OP27, OP32 and OP34 are indicated in colors. (a, b, c) oxidation air = 2 L/min and (d, e, f) mixing air = 0.1 L/min. Uncertainties account for 3 size distributions measured

consecutively. Data not corrected for dilution (~ 19:1).

Soot aggregates size distributions statistical descriptors

Table S.2.1. Aggregates number concentration (PN), mobility-equivalent geometric mean diameter ($D_{geo,m}$) and geometric standard deviation of size distributions displayed in Figure 4 for untreated and CS-treated conditions. Uncertainties account for 3 size distributions measured consecutively. Data not corrected for dilution (~ 19:1).

Operating point (OP)	PN [# /cm^3]		$D_{geo,m}$[nm]		σ_{geo,D_m}	
	Untreated	CS-treated	Untreated	CS-treated	Untreated	CS-treated
OP2	$3.9 \pm 0.6 \times 10^6$	$2.3 \pm 0.1 \times 10^6$	60.3 ± 3.6	57.6 ± 1.0	1.746 ± 0.035	1.738 ± 0.034
OP9	$1.1 \pm 0.0 \times 10^7$	$7.9 \pm 0.1 \times 10^6$	79.3 ± 0.2	79.1 ± 0.8	1.612 ± 0.007	1.604 ± 0.007
OP17	$1.3 \pm 0.0 \times 10^7$	$1.1 \pm 0.0 \times 10^7$	96.0 ± 0.6	63.7 ± 0.5	1.632 ± 0.006	1.845 ± 0.007
OP27	$1.9 \pm 0.0 \times 10^7$	$1.3 \pm 0.0 \times 10^7$	92.9 ± 0.9	88.3 ± 0.9	1.661 ± 0.000	1.708 ± 0.004
OP32	$1.7 \pm 0.0 \times 10^7$	$1.2 \pm 0.0 \times 10^7$	74.2 ± 0.2	62.6 ± 0.9	1.643 ± 0.002	1.877 ± 0.024
OP34	$1.5 \pm 0.0 \times 10^7$	$1.2 \pm 0.0 \times 10^7$	62.3 ± 0.7	54.9 ± 0.3	1.597 ± 0.004	1.797 ± 0.004

Deposit on filters

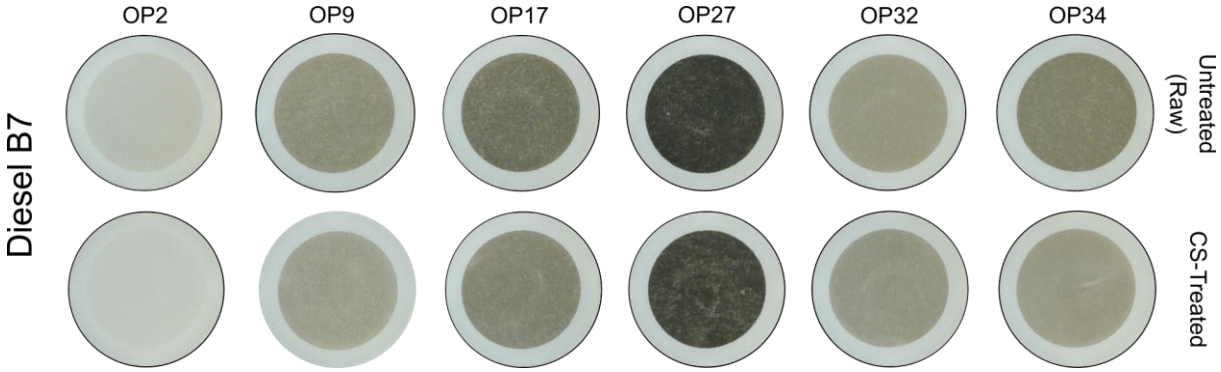

11.

Figure S.2.2. Soot aggregate samples deposited on borosilicate microfibers filters (Pallflex-Emfab, Pall Corp., U.S.A) generated under OP2, OP9, OP17, OP27, OP32 and OP34 operating points grouped using diesel B7 for both untreated (raw) and CS-treated

exhaust.

12. S.3.Electron microscopy diagnostic

Sampling conditions

Probing soot aggregates for electron microscopy imaging can be challenging because one must determine optimal sampling conditions to accommodate with soot PN variability. Conducting these experiments was done using a second dilution stage (see Figure 1) that allowed lowering soot PN therefore avoiding TEM grids overload. To help decide on sampling times, a preliminary investigation was conducted where soot aggregates produced under OP9 and OP27 (since they almost cover the lower and upper bounds of PN variation range) were probed under variable sampling times (10, 30 and 60 seconds) as summarized in Table S.3.1. Untreated exhaust diluted at ~ 220:1 was sampled at 20 mL/min using a Gilian, GilAir Plus (Sensidyne LP., U.S.A) pump positioned downstream the MPS tube. Scanning electron microscopy (SEM) observations shown in Figure S.3.1 were acquired using a SEM Crossbeam 350 (Zeiss GmbH., Germany) microscope, operated with an acceleration voltage of either 15, 25, or 30 kV with bright field detection using an aSTEM detector. These observations show that soot deposits were homogeneous within each sample and that no significant overload was observed. SEM observations also indicate that as sampling time increased, more particles are captured by TEM grids and that more particles are captured under OP27 compared to OP9 for similar sampling times which is coherent with the fact that under OP27 (at constant dilution ratio) more particles are generated compared to OP9 (see Figure S.3.1.a). Additionally, a blank sample was prepared last (no shown). The corresponding TEM grid seemed clean compared to loaded ones although some particles are still observed in few regions of the grid. However, their distribution is absolutely not homogeneous which leads to believe that such contamination is minor. As for optimal sampling times, it seemed that a proper number of aggregate deposits was obtained at 30-seconds and 10-seconds for OP9 and OP27, respectively. Furthermore, as combustion exhaust are diluted well after being produced in the burner's flame, soot aggregates are considered already mature. Therefore, even though the dilution

process might slightly impact aggregate size distribution for some OPs (as seen in section S.1), morphological parameters are assumed to be invariant in respect to the dilution process as suggested by Ouf et al. 2010.

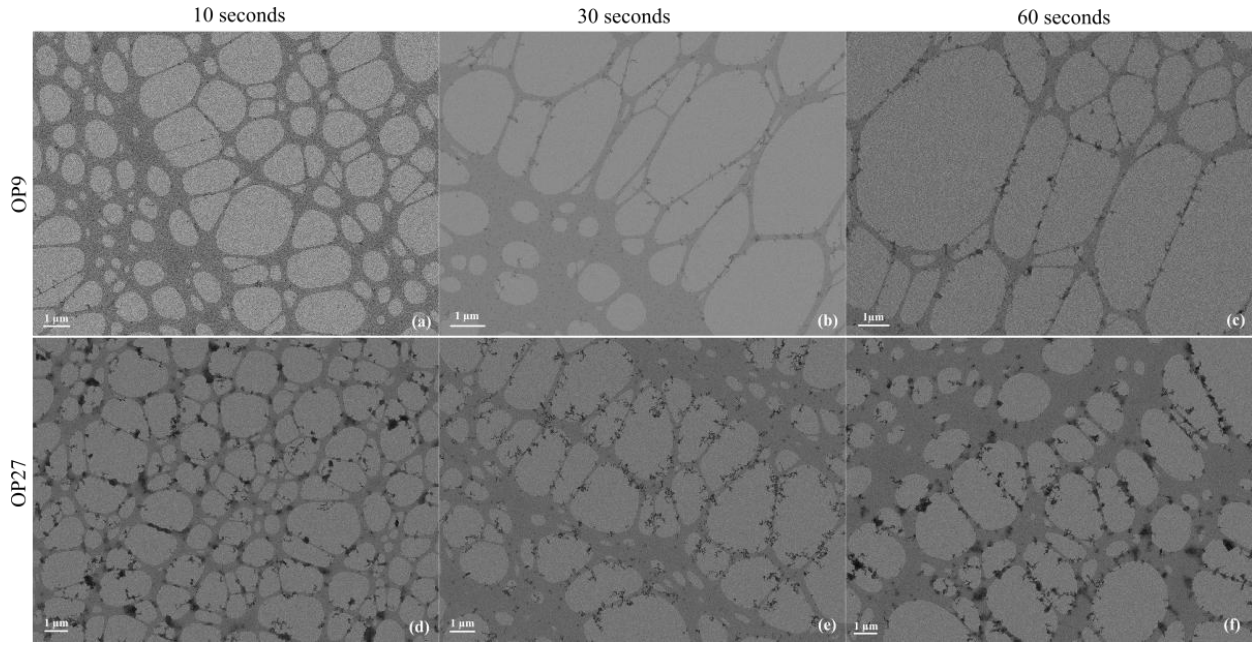

Figure S.3.1. Scanning electron microscopy (SEM) images of representative miniCAST soot aggregates deposited on Au holey carbon film (300 mesh) TEM grids, for untreated exhaust under (a, b, c) OP9 and (d, e, f) OP27 for for (a,d) 10-seconds, (b,e) 30-seconds and (c,f) 60-seconds.

Table S.3.1. Soot aggregates sampling conditions for the preliminary investigation. Soot deposits were done on Au holey carbon film (300 mesh) TEM grids.

Operating point (OP)	Condition	Sampling flow rate [mL/min]	Sampling time [s]	Global dilution ratio
OP9	Untreated	20	10	220:1
OP9	Untreated	20	30	220:1
OP9	Untreated	20	60	220:1
OP27	Untreated	20	10	220:1
OP27	Untreated	20	30	220:1

OP27	Untreated	20	60	220:1
Blank (under idle)	Untreated	20	60	220:1

Consequently, sampling times summarized in Table S.3.2 were determined considering soot PN for each of the selected operating points/conditions. According to the experimental protocol detailed in section 2.1.2., STEM and TEM images were acquired. The following subsections will focus on using STEM images to extract soot morphological parameters.

Table S.3.2. MiniCAST setting and exhaust sampling conditions for STEM and TEM and electron microscopy imaging diagnostics.

Operating point (OP)	**Condition**	**Sampling flow rate [mL/min]**	**Sampling time [s]**	**Global dilution ratio**
OP2	Untreated	20	40	220:1
OP9	Untreated	20	30	220:1
OP17	Untreated	20	15	220:1
OP27	Untreated	20	10	220:1
OP32	Untreated	20	10	220:1
OP34	Untreated	20	10	220:1
OP9	CS-treated	20	40	220:1
OP27	CS-treated	20	20	220:1
OP34	CS-treated	20	15	220:1

STEM images analysis

Retrieving aggregate morphological parameters ($D_{geo,p}$, σ_{geo,D_p}, D_f and k_f) from electron microscopy images is a challenging task for many reasons, first of which is the sampling media made of a carbon film that makes it difficult to get aggregates with enough contrast with the background and second, resulting from the sampling protocol itself that uses MPS, where perforated TEM grids are needed, in contrast to thermophoretic sampling that are usually used (Migliorini et al. 2011; Yon et al. 2011; Lee et al. 2008; Tian et al. 2004) to probe soot aggregates in a flame using filled TEM grids instead. Consequently, this making it even more difficult as the background is not restricted to the carbon film itself but could also be void as shown in Figure S.3.1. The main goal of the following analysis is to retrieve aggregate morphological parameters from STEM microscopy images. This was achieved following four major post processing steps that begins by segmenting raw STEM

images into single binary aggregates. To overcome background-related issues, the choice was made to use a semi-automated method (i.e., SLIDER method (Sipkens and Rogak 2021)) allowing the user to intervene, when necessary, to help indicate an aggregate border. Then, a second post processing (i.e., EDM-SBS (Bescond et al. 2014)) was performed on each single aggregate providing information (i.e., S(D) functions so-called EDM-SBS functions) encompassing scales encountered in each single aggregate. That same information was then interpreted to evaluate soot aggregates the geometric mean diameter of primary particles ($D_{geo,p}$,) and geometric standard deviation (σ_{geo,D_p}) following an approach proposed by Bescond et al. 2014. Finally, a fractal analysis was conducted in order to evaluate both fractal dimension (D_f) and fractal prefactor (k_f). The following paragraphs will therefore detail each of these steps, explaining the hypotheses that were made and discussing related uncertainties.

Segmentation process

Considering the nature of STEM images acquired in this work, automated segmentation methods proved to be inefficient due to difficulties in distinguishing aggregates from the background. Consequently, segmentation was done using a largely-manual method, wherein the threshold is adjusted with a SLIDER in a Graphical User Interface (GUI) (Sipkens et al. 2021). This method offered the possibility of adjusting a threshold on small regions in each image. The segmentation process is illustrated on an example in Figure S.3.2, where the SLIDER method is applied on raw STEM images of aggregates obtained under OP9 for an untreated exhaust (see Figure S.3.2.a), thus indicating each aggregate contour (see Figure S.3.2.b) after SLIDER method was applied. All truncated aggregates were systematically discarded. Rendered binary images resulting from the determined contours of each single aggregate were then generated (see Figure S.3.2.c), where aggregates are shown in white. Then, each aggregate was identified, isolated and inverted (see Figure S.3.2.d). The uncertainty of determining an aggregate projected surface was calculated based on the edge pixels (Sipkens et al. 2021). Accordingly, if one considers an average error of 2 pixels on the border, which is equivalent to adding or subtracting twice the perimeter from the overall area, then the percent error in the area would be 1-

(A $\pm$ 2P)/A where P is the number of perimeter pixels and A the total number of pixels considered in each aggregate (Sipkens et al. 2021). Consequently, when the image quality allowed it, care was taken to keep that uncertainty as low as possible.

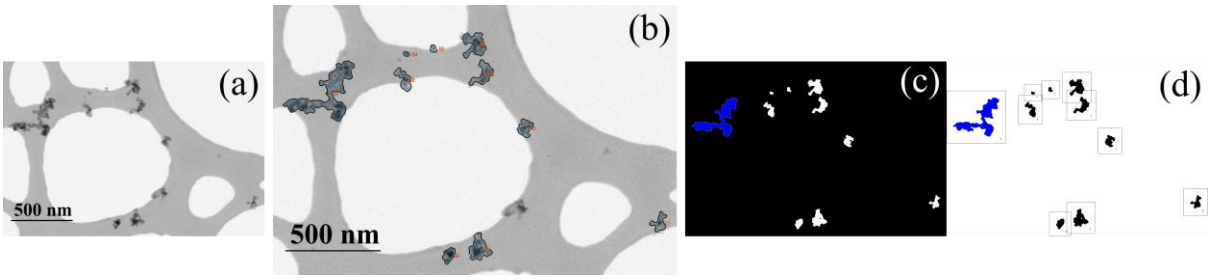

Figure S.3.2**.** Segmentation process showing example of (a) raw STEM image, (b) aggregates contours obtained using SLIDER method (Sipkens and Rogak 2021), (c) the corresponding binary image and (d) isolated aggregates after being inverted. This example corresponds to aggregates obtained under OP9 for untreated exhaust.

On average, 20 STEM images were processed per configuration. As each image contained more than 5 aggregates, on average more than 150 single aggregate per configuration were successfully retrieved with a satisfying error on aggregate area of at best ~ 7 % and at worse ~ 11 % as summarized in Table 2. In respect to similar studies from literature (Sipkens et al. 2021; Bescond et al. 2014), this was considered to be sufficient enough for a statistically representative result.

EDM-SBS process

The following processing step consist of applying Euclidian Distance Mapping-Surface Based Scale (EDM-SBS) method proposed by Bescond et al. 2014. This approach consists of applying series of image transformations, where each single aggregate area (S) is progressively eroded. Consequently, eroded surface areas may be computed as a function of the erosion level (k). The EDM-SBS then consists of studying the dependence of the eroded surface area to erosion magnitude. Figure S.3.3 shows a summary of these image transformations applied on the blue aggregate in Figure S.3.2.d.

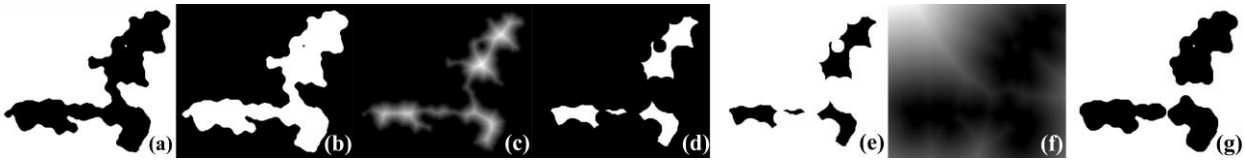

Figure S.3.3**.** EDM-SBS protocol (Bescond et al. 2014) applied on the blue aggregate of Figure S.3.2. The protocol consists of taking a binary image of an isolated aggregate (a), whose area is$S_{k=0}$, inverting it (b), and getting its corresponding Euclidian distance map (EDM) (c). The process continues through a loop over 'k' gray levels of the EDM image and applying a threshold at level 'k' to get an eroded surface hence image (d), inverting it to get image (e) reapplying an EDM calculation to get image (f) and reapplying a threshold at level 'k' – this is equivalent to a dilatation of the previous eroded surface – hence getting image (g), whose area is S_k. Images (d), (e), (f) and (g) show the example of level k = 10.

During this process, each single aggregate binary image goes through multiple transformations beginning with computing its initial surface area $S_{k=0}$ corresponding to the black area of Figure S.3.3.a. This image is first inverted as shown in Figure S.3.3.b, therefore allowing to render its corresponding distance map as shown in Figure S.3.3.c. The latter is a level of gray image representing the smallest distance to the border within the aggregate. The protocols continue through a loop over 'k' gray levels, where each time a threshold at that 'k' level is applied on its corresponding distance map image. This results in an eroded surface, for instance at k = 10 as shown in Figure S.3.3.d. The resulting images is then inverted before reapplying the same process (i.e., EDM calculation and thresholding at same 'k' level) once more. As mentioned before, EDM-SBS approach consists of studying the dependence of S_k as a function of the scale 2k+1 (Bescond et al. 2014). Knowing that the image resolution is ~ 0.725 pixels/nm, it is then possible to deduce a surface S(D) at each scale diameter (D) using the following conversions:

$$D = \frac{2k + 1}{\text{Resolution}} \qquad \text{(Eq.S.3.1)}$$

$$S = \frac{N_{pixels}}{Resolution^2} \qquad \text{(Eq.S.3.2)}$$

The EDM-SBS process described before was then applied to the rest of the investigated configurations resulting in normalized mean EDM-SBS function (S(D)/S(0)) similar to the one displayed in Figure S.3.4 which are used to evaluate the geometric mean primary particle diameter ($D_{geo,p}$) and a standard geometric deviation (σ_{geo,D_p}) describing primary particles size distributions.

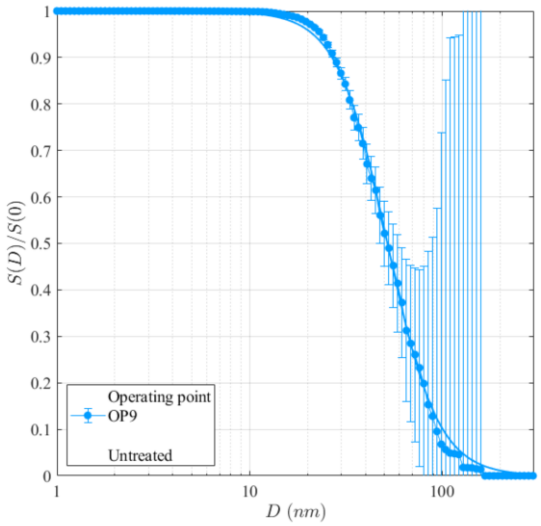

Figure S.3.4. Representation of the normalized mean EDM-SBS function against the scale diameter D resulting for EDM-SBS analysis N = 198 soot aggregates produced under OP9 for untreated exhaust.

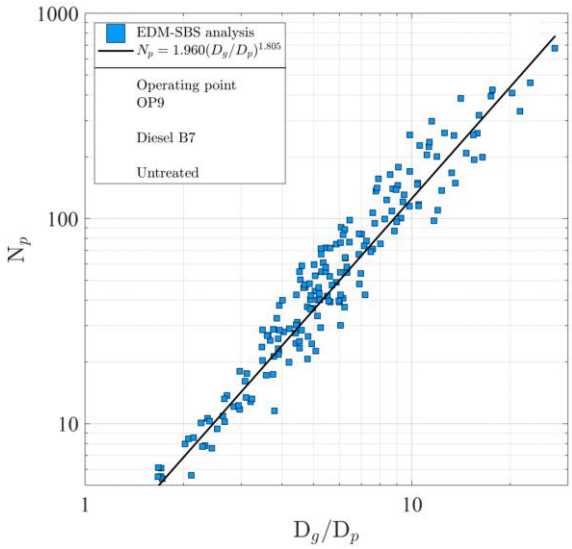

Figure S.3.5. Evolution of number of primary particles per aggregate N_p as a function of D_g/D_p ratio based on EDM-SBS analysis considering 198 single aggregates produced under OP9 for untreated exhaust.

Normalized mean EDM-SBS function interpretation

The decay of S(D)/S(0) function, holds information on the different scales encountered in the images and therefore in the aggregates. To extract this information, Bescond et al.

2014 proposed many approaches to find an adequate model expressed as a function of $D_{geo,p}$ and σ_{geo,D_p} that allow to approximate S(D)/S(0) curves and thus to evaluate these two parameters. The first approach proposed was to consider that the aggregates are made of polydisperse spheres without overlap. This is how equation 4 (in Bescond et al. 2014) was proposed. To be more realistic, the authors proposed a second approach to take into account aggregates with complex shapes and overlapping/necking, hence the need to calibrate the S(D)/S(0) function on the basis of controlled soot. To do that, the authors worked first with virtual aggregates in contact point for which S(D)/S(0) functions were obtained. It was then concluded that these curves are superimposed when they are represented as a function of $X = (\ln(D)-\ln(D_{geo,p}))/\ln(\sigma_{geo,D_p})$. This is how the model in equation 5b (in Bescond et al. 2014) was proposed. However, when overlap effects were considered, this last observation was no longer valid, which led the authors to conclude that these curves have to be calibrated on real soot. Therefore, with this third approach, manually determined size distributions were obtained which were used to evaluate two calibration constants β at 1.90 ±0.03 and Ω at 0.80 ± 0.03 of a sigmoid law (Eq.S.3.3). The application of the latter approach on miniCAST propane soot allowed its validation against distributions obtained again in a manual way with the method of circles.

$$f(D) = \left(1 + \exp\left(\frac{\frac{\ln(D)-\ln(D_{geo,p})}{\ln(\sigma_{geo,D_p})} - \beta}{\Omega} \right) \right)^{-1} \qquad \text{(Eq.S.3.3)}$$

When this final approach was applied in this work, the fitting of S(D)/S(0), assuming β = 1.90 and Ω = 0.80 as proposed by Bescond et al. 2014 resulted in overestimating $D_{geo,p}$ (by ~ 10 nm) with respect to a $D_{geo,p}$ obtained manually. Consequently, the calibration constants β and Ω were reevaluated considering the case of OP34 for untreated exhaust since it presented the lowest error on aggregate area. For this condition, 506 primary particles were determined manually from STEM images (using Image J software) allowing to build a primary particles size distribution (not shown). As such, $D_{geo,p}$ and σ_{geo,D_p} were

determined, and then β and Ω were reevaluated. This resulted in Ω = 0.6699 ± 0.009 and β = 2.1636 ± 0.012. These same calibration constants were then used for the rest of the studied conditions to evaluate $D_{geo,p}$ and σ_{geo,D_p} as summarized in Table 2.

Fractal analysis

After determining the diameters of soot primary particles, here it is proposed to evaluate the remaining parameters describing soot aggregates morphology which are the fractal dimension (D_f) and the fractal prefactor (k_f). To evaluate those two parameters, two laws are used. The first one is the fractal law (Eq.2) expressing the number of primary particles per aggregate (N_p) as a function of the aggregate gyration diameter (D_g) and the diameter of soot primary particles (D_p). In the previous processing step, primary particles were considered polydisperse. For the sake of simplicity, primary particles are from now on considered monodisperse with a mean primary particle diameter $\overline{D_p} \approx D_{geo,p}$.The second law is taken from the previous works of Samson et al. 1987 and Köylü et al. 1995 who suggested to link N_p to aggregates projected area. As such, (Eq.S.3.4) was proposed where $k_a$is the prefactor projected area, A_a is the aggregate projected area, A_p is the primary particle projected area and α_a is the projected area exponent.

$$N_p = k_a \left(\frac{A_g}{A_p}\right)^{\alpha_a} \qquad \text{(Eq.S.3.4)}$$

Following Bescond et al. 2014 approach, using (Eq.S.3.4) by (i) assuming k_a = 1.155 and α_a = 1.095 as suggested by Köylü et al. 1995 and Sorensen and Roberts 1997, (ii) computing gyration diameter (D_g) using L/D_g = 1.49 correlation as proposed by Köylü et al. 1995 (L being the projected maximum length of an aggregate) which is very close to the values of 1.48 used by Yon et al. 2011 and of 1.50 used by Brasil et al. 1999 and (iii) constraining the problem with $k_f \propto ((D_f + 2)/ D_f)^{D_f/2}$ as suggested by Sorensen and Roberts 1997 both D_f and k_f were evaluated by means of a least-square minimization algorithm. Accordingly, Figure S.3.5 shows the fractal analysis results for OP9 for untreated exhaust. As this Figure shows, care was taken to consider a wide range of aggregate sizes

for each case and the fitting procedure was applied accounting only for data points with N_p > 5. With such log-log representation D_f and k_f can easily be linked to the slope and intercept of the cloud points. Accordingly, Table 2 recapitulates evaluated D_f and k_f values for all studied configurations.

Impact of the catalytic stripper

Figure S.3.6 **s**hows STEM, and TEM images of representative miniCAST soot aggregates for a CS-treated exhaust obtained under OP9, OP27 and OP34. Soot morphological parameters for these conditions were evaluated by analyzing their corresponding STEM images as summarized in Table 2.

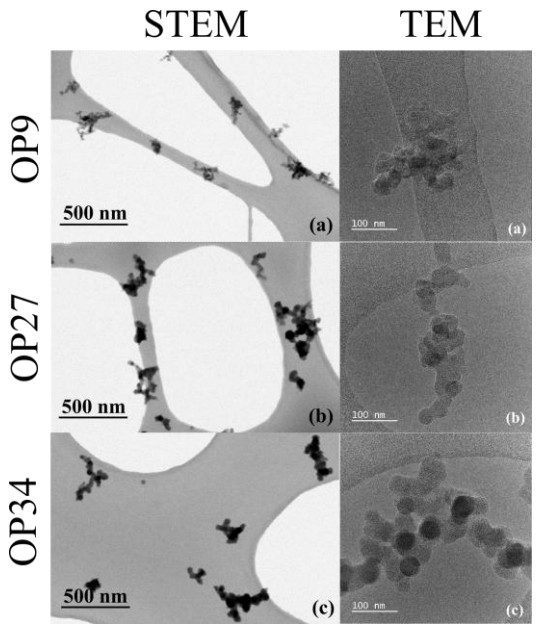

Figure S.3.6. Scanning transmission electron microscopy (STEM) (left row) and transmission electron microscopy (TEM) (right row) images of representative miniCAST soot aggregates for CS-treated exhaust obtained under (a) OP9, (b) OP27 and (c) OP34.

Mean primary particles diameters

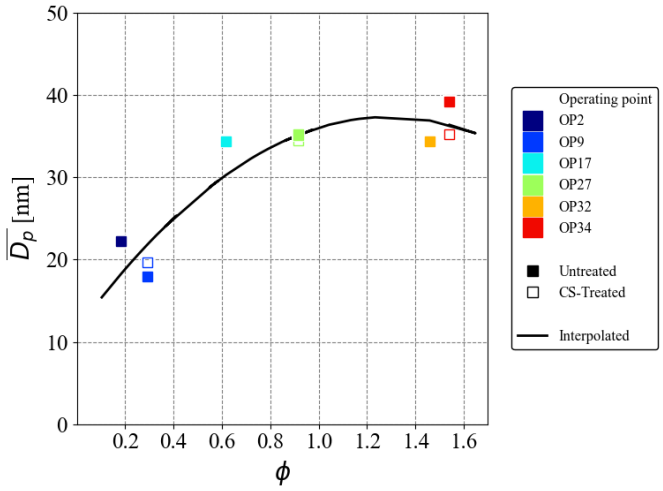

Figure S.3.7. Evaluated mean primary particles diameter ($\overline{D_p}$) reported in Table 2 as a function of flame overall equivalence ratio (ϕ). The straight line indicates interpolated $\overline{D_p}$ for the 34 other OPs as a function of ϕ.

13. S.4.Gas phase and total scattering contribution to extinction

In this work, the optical absorption coefficients of all absorbing molecular species ($\sum_i K_{abs,i}$) in the gas phase were measured only for a selection of operating conditions (e.g., untreated exhaust obtained under OP2, OP9, OP17, OP27, OP32 and OP34 shown in Figure 7). Since this gas phase only absorbs UV light (< 400 nm), for all investigated OPs, it is assumed that above 400 nm $K_{ext} \approx K_{ext,soot}$. Here, it is proposed to use the RDG-FA model (Bohren and Huffman 1983) (Eq.S.4.1) to evaluate the total scattering contribution in $K_{ext,soot}$. With $\overline{D_p} \sim 17$ nm Yon et al. 2011 reported a contribution of total scattering in extinction of ~ 7 % at λ = 370 nm. Similarly, Migliorini et al. 2011 estimated that the maximum contribution for total scattering can reach up to 8 % at λ = 450 nm and drops for higher wavelengths. As $\overline{D_p}$ increases this contribution is expected to increase furthermore.

$$K_{ext,soot} = K_{abs,soot} + K_{sca,soot}$$

$$K_{ext,soot} = \frac{\pi^2 \overline{D_p}^3 PN}{\lambda} E(m) \int_0^{\infty} N_p \, n(D_g) dD_g + \frac{2\pi^5 \overline{D_p}^6 PN}{3\lambda^4} F(m) \int_0^{\infty} {N_p}^2 g(D_g, \lambda, D_f) n(D_g) dD_g \quad \text{(Eq.S.4.1)}$$

$$K_{ext,soot} = \frac{6\pi E(m)}{\lambda} f_v + \frac{2\pi^5 \overline{D_p}^6 PN}{3\lambda^4} F(m) \int_0^{\infty} {N_p}^2 g(D_g, \lambda, D_f) n(D_g) dD_g$$

According to the RDG-FA model (Eq.S.4.1), $K_{sca,soot}$ is insignificant as long as soot aggregates verify the Rayleigh limit (Dobbins and Megaridis 1991): $x_p = \pi \overline{D_p} / \lambda << 1$. For instance, under OP9 and OP27, $\overline{D_p}$ were evaluated to 18 nm and ~ 35 nm, respectively which means that at 400 nm, x_p = 0.14 and 0.27 for OP9 and OP27, respectively. Under such conditions, neglecting total scattering contribution might be judged inconsistent. Distinguishing $K_{sca,soot}$ from $K_{abs,soot}$ is not feasible relying solely on light extinction measurement. Even if aggregates number, size and morphology are unequivocally determined, the absorption and scattering functions E(m) and F(m) remain unknown functions. This shortfall can be compensated using models such as Lorentz-Drudes (Bohren and Huffman 1983) that uses dispersion relations for optical refractive index of soot. Combined with the previous mentioned aggregates descriptors and a measurement of $K_{ext,soot}$, E(m) and F(m) functions can be estimated. Proceeding accordingly, for soot aggregates generated by a McKenna hybrid burner using a diesel fuel, Yon et al. 2011 found that F(m) depended much less on the wavelength in the range 380 < λ [nm] < 1000 recommending a value of F(m) = 0.31 $\pm$ 0.08. Later, Bescond et al. 2016 applied a similar approach while additionally accounting for the effect of internal multiple scattering in evaluating E(m) and F(m). In their study that concerned soot aggregates generated by a miniCAST burner supplied with propane, F(m) was found to vary, across the operating conditions, between 0.42 and 0.16 for 380 < λ [nm] < 1000 and with a less noticeable variation when approaching higher wavelengths (i.e., F(m) = 0.23 $\pm$ 0.06 at 700 nm). The objective here is not to evaluate the wavelength variations of E(m) and F(m) functions for

soot aggregates generated by a miniCAST burner supplied with diesel. Instead, it is proposed to use Yon et al. 2011 F(m) recommended value for 400 < λ [nm] < 1000 and the RDG-FA model (Eq.S.4.1) to estimate how much total scattering contribute to extinction. Multiscattering is neglected. Having measured aggregates size distribution and evaluated morphological key parameters, $K_{sca,soot}$ is estimated for OP9 and OP27. In this regard, an additional assumption is made to convert mobility diameters (measured in this work) to gyration diameters (needed for the RDG-FA model) using $\beta = D_g/D_m = 1.3$ for the reasons discussed in section 3.2.1. Consequently, Figure S.4.1 shows the estimated percentages of $K_{sca,soot}$ in $K_{ext,soot}$. With $\overline{D_p}$ = 18 nm, the contribution of total scattering in extinction under OP9 remains below 10 % in agreement with Yon et al. 2011 and Migliorini et al. 2011. However, looking at OP27's case, these calculations show that indeed for aggregates with higher $\overline{D_p}$ (~ 35 nm in this case) total scattering cannot necessarily be neglected as it reaches on average ~ 12 % at 400 nm. Therefore, assigning the extinction to be equal to the absorption has to be judged from case-to-case.

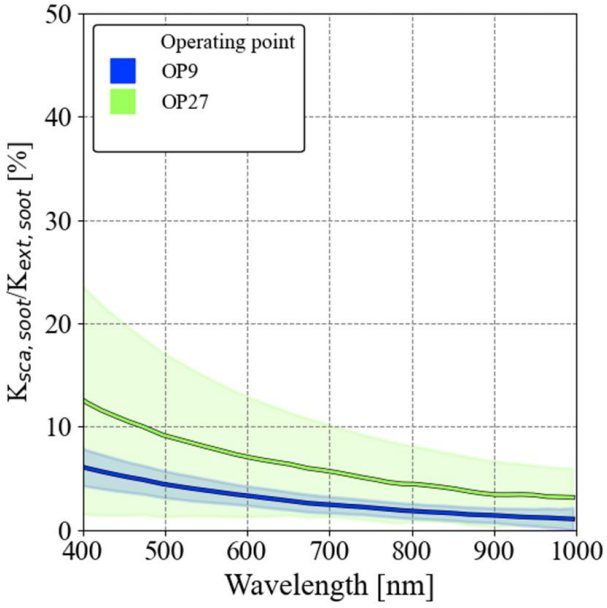

Figure S.4.1. Estimated percentages of total scattering in soot extinction coefficients for soot aggregates obtained under OP9 and OP27 (for an untreated exhaust), using RDG-FA

model incorporating aggregate size distribution and morphological parameters and assuming a constant scattering function F(m) = 0.31 for 400 < λ [nm] < 1000. Shadow areas corresponds to uncertainties accounting for $K_{ext,soot}$ measurement standard deviation and Δ F(m) = 0.08.

14. S.5.Overview of operating points characteristics

15.

Table S.5.1. Overview of soot aggregates characteristics (PN corrected for dilution, $D_{geo,m}$, σ_{geo,D_m}, $\overline{D_p}$, D_f and α*) of soot aggregates generated by a miniCAST burner for untreated exhaust using diesel B7. *Evaluated by fitting $K_{abs,soot}$ by a power law ($\lambda^{-\alpha}$) between 400 nm and 1000 nm accounting for total scattering. $\overline{D_p}$, values in gray are interpolated according to Figure S.3.7 while is D_f kept constant at 1.851.

Operating point (OP)	PN [#/cm³]	$D_{geo,m}$[nm]	σ_{geo,D_m}	$\overline{D_p}$[nm]	D_f	α*
OP1	7.1 ± 0.1 × 10^7	87.8 ± 1.0	1.671 ± 0.010	15.5	1.851	1.37
OP2	6.1 ± 0.7 × 10^7	45.0 ± 2.9	1.818 ± 0.013	22.3 ± 0.4	1.839	1.42 ± 0.04
OP3	1.2 ± 0.0 × 10^8	94.1 ± 0.6	1.597 ± 0.006	18.6	1.851	1.26
OP4	8.1 ± 0.2 × 10^7	49.8 ± 0.5	1.749 ± 0.008	18.9	1.851	-
OP5	1.1 ± 0.0 × 10^8	60.5 ± 0.6	1.678 ± 0.012	19.5	1.851	-
OP6	1.3 ± 0.0 × 10^8	67.2 ± 1.6	1.631 ± 0.005	20.2	1.851	1.12
OP7	1.4 ± 0.0 × 10^8	72.4 ± 0.2	1.623 ± 0.011	21.1	1.851	1.14
OP8	8.3 ± 0.2 × 10^7	53.4 ± 0.8	1.719 ± 0.011	21.9	1.851	-
OP9	1.4 ± 0.0 × 10^8	81.2 ± 1.6	1.590 ± 0.003	18.0 ± 0.4	1.805	1.32 ± 0.09
OP10	1.8 ± 0.1 × 10^8	80.4 ± 1.7	1.784 ± 0.004	22.5	1.851	1.52
OP11	1.8 ± 0.0 × 10^8	77.8 ± 0.6	1.571 ± 0.006	23.4	1.851	1.05

OP12	$2.3 \pm 0.1 \times 10^8$	67.7 ± 0.2	1.736 ± 0.011	25.5	1.851	1.77
OP13	$2.5 \pm 0.0 \times 10^8$	104.7 ± 0.1	1.516 ± 0.000	24.3	1.851	1.21
OP14	$2.7 \pm 0.0 \times 10^8$	79.3 ± 0.1	1.597 ± 0.002	29.7	1.851	1.57
OP15	$2.8 \pm 0.0 \times 10^8$	83.8 ± 0.5	1.616 ± 0.002	30.0	1.851	1.68
OP16	$3.2 \pm 0.1 \times 10^8$	88.6 ± 4.7	1.618 ± 0.026	29.0	1.851	1.51
OP17	$2.7 \pm 0.1 \times 10^8$	67.0 ± 2.7	1.700 ± 0.015	34.4 ± 0.3	1.941	1.72 ± 0.20
OP18	$3.1 \pm 0.0 \times 10^8$	89.1 ± 0.2	1.673 ± 0.001	32.5	1.851	1.45
OP19	$3.3 \pm 0.0 \times 10^8$	78.8 ± 0.2	1.715 ± 0.002	32.8	1.851	1.56
OP20	$3.1 \pm 0.0 \times 10^8$	91.2 ± 0.4	1.708 ± 0.007	33.1	1.851	1.35
OP21	$3.4 \pm 0.1 \times 10^8$	85.6 ± 0.3	1.710 ± 0.009	33.7	1.851	1.57
OP22	$3.2 \pm 0.1 \times 10^8$	57.5 ± 0.2	1.630 ± 0.014	34.7	1.851	2.19
OP23	$3.5 \pm 0.0 \times 10^8$	64.5 ± 0.3	1.590 ± 0.003	35.0	1.851	2.12
OP24	$3.3 \pm 0.0 \times 10^8$	81.6 ± 1.3	1.713 ± 0.003	34.7	1.851	1.66
OP25	$3.1 \pm 0.0 \times 10^8$	67.4 ± 0.3	1.648 ± 0.008	35.4	1.851	1.70
OP26	$3.4 \pm 0.0 \times 10^8$	80.8 ± 0.5	1.709 ± 0.007	35.7	1.851	1.65
OP27	$3.7 \pm 0.1 \times 10^8$	70.3 ± 1.8	1.685 ± 0.011	35.2 ± 0.2	1.831	1.68 ± 0.03
OP28	$3.3 \pm 0.0 \times 10^8$	75.6 ± 0.0	1.711 ± 0.005	36.6	1.851	1.75
OP29	$3.0 \pm 0.0 \times 10^8$	57.7 ± 0.7	1.709 ± 0.020	37.1	1.851	1.94
OP30	$3.4 \pm 0.0 \times 10^8$	60.1 ± 0.4	1.615 ± 0.005	37.2	1.851	1.99
OP31	$3.3 \pm 0.0 \times 10^8$	68.4 ± 0.1	1.630 ± 0.001	37.3	1.851	1.83
OP32	$3.5 \pm 0.0 \times 10^8$	59.7 ± 0.2	1.620 ± 0.006	34.4 ± 0.4	1.862	2.06 ± 0.12
OP33	$3.7 \pm 0.0 \times 10^8$	60.9 ± 0.1	1.552 ± 0.003	35.1	1.851	2.25
OP34	$3.4 \pm 0.0 \times 10^8$	69.5 ± 0.2	1.623 ± 0.003	39.2 ± 0.2	1.844	2.01 ± 0.17

16.

Table S.5.2. Overview of soot aggregates characteristics (PN corrected for dilution, $D_{geo,m}$, σ_{geo,D_m}, $\overline{D_p}$, D_f and α^*) of soot aggregates generated by a miniCAST burner for CS-treated exhaust using diesel B7. *Evaluated by fitting $K_{abs,soot}$ by a power law ($\lambda^{-\alpha}$) between 400 nm and 1000 nm accounting for total scattering. $\overline{D_p}$, values in gray are interpolated according to Figure S.3.7 while is D_f kept constant at 1.851.

Operating point (OP)	**PN [#/cm³]**	**$D_{geo,m}$[nm]**	**σ_{geo,D_m}**	**$\overline{D_p}$[nm]**	**D_f**	α^*
OP1	5.9 ± 0.0 × 10^7	89.3 ± 0.8	1.667 ± 0.014	15.5	1.851	1.31
OP2	6.1 ± 0.1 × 10^7	49.2 ± 1.0	1.701 ± 0.031	18.4	1.851	-
OP3	1.0 ± 0.1 × 10^7	100.9 ± 0.5	1.548 ± 0.007	18.6	1.851	1.26
OP4	5.9 ± 0.3 × 10^7	53.1 ± 1.2	1.683 ± 0.037	18.9	1.851	-
OP5	6.8 ± 0.2 × 10^7	58.1 ± 0.7	1.666 ± 0.007	19.5	1.851	-
OP6	8.5 ± 0.1 × 10^7	65.2 ± 0.6	1.619 ± 0.006	20.2	1.851	1.22
OP7	1.0 ± 0.0 × 10^8	72.3 ± 0.5	1.589 ± 0.006	21.1	1.851	1.11
OP8	7.1 ± 0.1 × 10^7	55.3 ± 0.7	1.682 ± 0.016	21.9	1.851	-
OP9	1.1 ± 0.0 × 10^8	80.9 ± 0.2	1.596 ± 0.004	19.7 ± 0.3	1.849	1.26 ± 0.15
OP10	1.3 ± 0.0 × 10^8	82.6 ± 0.1	1.821 ± 0.004	22.5	1.851	1.34
OP11	1.5 ± 0.0 × 10^8	80.1 ± 0.9	1.563 ± 0.014	23.4	1.851	1.16
OP12	1.7 ± 0.0 × 10^8	61.1 ± 0.7	1.784 ± 0.008	25.5	1.851	1.51
OP13	2.0 ± 0.1 × 10^8	100.3 ± 0.4	1.544 ± 0.003	24.3	1.851	1.22
OP14	1.5 ± 0.4 × 10^8	75.4 ± 1.1	1.630 ± 0.004	29.7	1.851	1.24
OP15	2.1 ± 0.0 × 10^8	81.8 ± 1.1	1.641 ± 0.010	30.0	1.851	1.38
OP16	2.3 ± 0.1 × 10^8	95.5 ± 0.8	1.627 ± 0.023	29.0	1.851	1.25
OP17	1.9 ± 0.0 ×	68.0 ± 1.1	1.849 ±	30.5	1.851	1.44 ± 0.03

	10^8		0.002			
OP18	2.2 ± 0.0 × 10^8	86.2 ± 0.3	1.690 ± 0.005	32.5	1.851	1.18
OP19	2.3 ± 0.0 × 10^8	87.9 ± 0.4	1.694 ± 0.003	32.8	1.851	1.23
OP20	2.3 ± 0.0 × 10^8	86.8 ± 0.9	1.759 ± 0.010	33.1	1.851	1.17
OP21	2.3 ± 0.0 × 10^8	86.3 ± 0.1	1.709 ± 0.001	33.7	1.851	1.22
OP22	2.3 ± 0.0 × 10^8	45.9 ± 0.9	1.763 ± 0.015	34.7	1.851	1.66
OP23	2.4 ± 0.0 × 10^8	52.2 ± 1.2	1.723 ± 0.017	35.0	1.851	1.51
OP24	2.2 ± 0.1 × 10^8	82.4 ± 0.2	1.744 ± 0.006	34.7	1.851	1.22
OP25	2.3 ± 0.0 × 10^8	54.1 ± 0.6	1.814 ± 0.009	35.4	1.851	1.45
OP26	2.2 ± 0.1 × 10^8	77.3 ± 0.2	1.770 ± 0.004	35.7	1.851	1.24
OP27	2.4 ± 0.0 × 10^8	87.6 ± 0.5	1.718 ± 0.001	34.5 ± 0.3	1.790	1.22 ± 0.05
OP28	2.1 ± 0.0 × 10^8	68.5 ± 0.0	1.811 ± 0.005	36.6	1.851	1.25
OP29	2.2 ± 0.0 × 10^8	56.0 ± 0.2	1.863 ± 0.007	37.1	1.851	1.30
OP30	2.3 ± 0.1 × 10^8	53.9 ± 2.5	1.844 ± 0.019	37.2	1.851	1.28
OP31	2.4 ± 0.0 × 10^8	57.0 ± 0.9	1.816 ± 0.012	37.3	1.851	1.35
OP32	2.3 ± 0.0 × 10^8	52.4 ± 0.1	1.869 ± 0.004	36.7	1.851	1.27 ± 0.10
OP33	2.0 ± 0.0 × 10^8	42.5 ± 0.5	1.796 ± 0.003	35.1	1.851	1.41
OP34	2.4 ± 0.0 × 10^8	55.4 ± 0.4	1.861 ± 0.002	35.2 ± 0.3	1.834	1.45 ± 0.21

References

Bescond, A., Yon, J., Ouf, F.X., Ferry, D., Delhaye, D., Gaffié, D., Coppalle, A., and Rozé, C. (2014). Automated Determination of Aggregate Primary Particle Size Distribution by TEM Image Analysis: Application to Soot. *Aerosol Sci. Technol.* 48 (8):831–841.

Bescond, A., Yon, J., Ouf, F.-X., Rozé, C., Coppalle, A., Parent, P., Ferry, D., and Laffon, C. (2016). Soot optical properties determined by analyzing extinction spectra in the

visible near-UV: Toward an optical speciation according to constituents and structure. *J. Aerosol Sci.* 101:118–132.

Bohren, C. and Huffman, D.R. (1983). Absorption and Scattering of Light by Small Particles. Wiley Science Paperback Series.

Brasil, A.M., Farias, T.L., and Carvalho, M.G. (1999). A recipe for image characterization of fractal-like aggregates. *J. Aerosol Sci.* 30 (10):1379–1389.

Dobbins, R.A. and Megaridis, C.M. (1991). Absorption and scattering of light by polydisperse aggregates. *Appl. Opt.* 30 (33):4747.

Köylü, U.O., Faeth, G.M., Farias, T.L., and Carvalho, M.G. (1995). Fractal and projected structure properties of soot aggregates. *Combust. Flame* 100 (4).

Lee, J., Altman, I., and Choi, M. (2008). Design of thermophoretic probe for precise particle sampling. *J. Aerosol Sci.* 39 (5):418–431.

Migliorini, F., Thomson, K.A., and Smallwood, G.J. (2011). Investigation of optical properties of aging soot. *Appl. Phys. B* 104 (2):273–283.

Ouf, F.X., Yon, J., Ausset, P., Coppalle, A., and Maillé, M. (2010). Influence of Sampling and Storage Protocol on Fractal Morphology of Soot Studied by Transmission Electron Microscopy. *Aerosol Sci. Technol.* 44 (11):1005–1017.

Samson, R.J., Mulholland, G.W., and Gentry, J.W. (1987). Structural analysis of soot agglomerates. *Langmuir* 3 (2):272–281.

Sipkens, T.A., Frei, M., Baldelli, A., Kirchen, P., Kruis, F.E., and Rogak, S.N. (2021). Characterizing soot in TEM images using a convolutional neural network. *Powder Technol.* 387:313–324.

Sipkens, T.A. and Rogak, S.N. (2021). Technical note: Using k-means to identify soot aggregates in transmission electron microscopy images. *J. Aerosol Sci.* 152:105699.

Sorensen, C.M. and Roberts, G.C. (1997). The Prefactor of Fractal Aggregates. *J. Colloid Interface Sci.* 186 (2):447–452.

Tian, K., Liu, F., Thomson, K.A., Snelling, D.R., Smallwood, G.J., and Wang, D. (2004). Distribution of the number of primary particles of soot aggregates in a nonpremixed laminar flame. *Combust. Flame* 138 (1):195–198.

Yon, J., Lemaire, R., Therssen, E., Desgroux, P., Coppalle, A., and Ren, K.F. (2011). Examination of wavelength dependent soot optical properties of diesel and diesel/rapeseed methyl ester mixture by extinction spectra analysis and LII measurements. *Appl. Phys. B* 104 (2):253–271.